[C II] AND 12CO(1–0) EMISSION MAPS IN HLSJ091828.6+514223: A STRONGLY LENSED INTERACTING SYSTEM AT $z = 5.24$

T. D. RAWLE[1,2], E. EGAMI[2], R. S. BUSSMANN[3], M. GURWELL[3], R. J. IVISON[4], F. BOONE[5], F. COMBES[6], A. L. R. DANIELSON[7], M. REX[2], J. RICHARD[8], I. SMAIL[7], A. M. SWINBANK[7], B. ALTIERI[1], A. W. BLAIN[9], B. CLEMENT[2], M. DESSAUGES-ZAVADSKY[10], A. C. EDGE[7], G. G. FAZIO[3], T. JONES[11], J.-P. KNEIB[12], A. OMONT[13], P. G. PÉREZ-GONZÁLEZ[2,14], D. SCHAERER[10,15], I. VALTCHANOV[1], P. P. VAN DER WERF[16], G. WALTH[2], M. ZAMOJSKI[10], AND M. ZEMCOV[17,18]

[1] ESAC, ESA, P.O. Box 78, Villanueva de la Cañada, E-28691 Madrid, Spain; tim.rawle@sciops.esa.int
[2] Steward Observatory, University of Arizona, 933 N. Cherry Ave., Tucson, AZ 85721, USA
[3] Harvard-Smithsonian Center for Astrophysics, 60 Garden Street, Cambridge, MA 02138, USA
[4] Institute for Astronomy, University of Edinburgh, Royal Observatory, Blackford Hill, Edinburgh EH9 3HJ, UK
[5] Université de Toulouse, UPS-OMP, CNRS, IRAP, 9 Av. Colonel Roche, BP 44346, F-31028 Toulouse Cedex 4, France
[6] Observatoire de Paris, LERMA, CNRS, 61 Av. de l'Observatoire, F-75014 Paris, France
[7] Institute for Computational Cosmology, Durham University, South Road, Durham DH1 3LE, UK
[8] CRAL, Université Lyon-1, 9 Av. Charles Andr, F-69561 St Genis Laval, France
[9] Department of Physics & Astronomy, University of Leicester, University Road, Leicester LE1 7RH, UK
[10] Observatoire de Genève, Université de Genève, 51 Ch. des Maillettes, 1290, Sauverny, Switzerland
[11] Department of Physics, University of California, Santa Barbara, CA 93106, USA
[12] Laboratoire d'Astrophysique EPFL, Observatoire de Sauverny, Versoix 1290, Switzerland
[13] 13 Institut d'Astrophysique de Paris, CNRS and UPMC Univ. Paris 06, UMR7095, 98bis Bd Arago, F-75014 Paris, France
[14] Departamento de Astrofísica, Facultad de CC. Físicas, Universidad Complutense de Madrid, E-28040 Madrid, Spain
[15] CNRS, IRAP, 14 Avenue E. Belin, F-31400 Toulouse, France
[16] Leiden Observatory, Leiden University, P.O. Box 9513, 2300 RA Leiden, The Netherlands
[17] California Institute of Technology, Pasadena, CA 91125, USA
[18] Jet Propulsion Laboratory, Pasadena, CA 91109, USA

ABSTRACT

We present Submillimeter Array [C II] 158 μm and Karl G. Jansky Very Large Array 12CO(1–0) line emission maps for the bright, lensed, submillimeter source at $z = 5.2430$ behind A 773: HLSJ091828.6+514223 (HLS0918). We combine these measurements with previously reported line profiles, including multiple 12CO rotational transitions, [C I], water, and [N II], providing some of the best constraints on the properties of the interstellar medium in a galaxy at $z > 5$. HLS0918 has a total far-infrared (FIR) luminosity $L_{\rm FIR(8-1000\,\mu m)} = (1.6 \pm 0.1) \times 10^{14}\, L_\odot\, \mu^{-1}$, where the total magnification $\mu_{\rm total} = 8.9 \pm 1.9$, via a new lens model from the [C II] and continuum maps. Despite a HyLIRG luminosity, the FIR continuum shape resembles that of a local LIRG. We simultaneously fit all of the observed spectral line profiles, finding four components that correspond cleanly to discrete spatial structures identified in the maps. The two most redshifted spectral components occupy the nucleus of a massive galaxy, with a source-plane separation <1 kpc. The reddest dominates the continuum map (demagnified $L_{\rm FIR, component} = (1.1 \pm 0.2) \times 10^{13}\, L_\odot$) and excites strong water emission in both nuclear components via a powerful FIR radiation field from the intense star formation. A third star-forming component is most likely a region of a merging companion ($\Delta V \sim 500$ km s^{-1}) exhibiting generally similar gas properties. The bluest component originates from a spatially distinct region and photodissociation region analysis suggests that it is lower density, cooler, and forming stars less vigorously than the other components. Strikingly, it has very strong [N II] emission, which may suggest an ionized, molecular outflow. This comprehensive view of gas properties and morphology in HLS0918 previews the science possible for a large sample of high-redshift galaxies once ALMA attains full sensitivity.

Key words: galaxies: high-redshift – galaxies: star formation – submillimeter: galaxies

Online-only material: color figures

1. INTRODUCTION

Atomic and molecular lines are particularly important diagnostics of star formation, active galactic nuclei (AGNs), and the interstellar medium (ISM), as the properties of the gas are dictated by the heating and cooling of various species. Furthermore, spectrally resolved emission line observations provide direct insight into the dynamics of a system.

The observed far-infrared (FIR) and submillimeter spectrum of an actively star-forming galaxy is dominated by emission lines originating in photodissociation regions (PDRs), the surfaces of molecular clouds exposed to the ionizing ultraviolet (UV) flux from nearby young stars. Carbon is both abundant and possesses a lower ionization potential than hydrogen (11.3 eV compared with 13.6 eV), making the [C II] 158 μm line a very

important coolant for regions with neutral hydrogen. Although [C II] principally traces the UV-irradiated molecular clouds, the line is largely unaffected by extinction in plausible local environments (although, see the discussion in, e.g., Gerin & Phillips 1998), making it an excellent diagnostic for the physical conditions of the neutral gas (e.g., Maiolino et al. 2005; Venemans et al. 2012). Any interpretation must also acknowledge that significant [C II] emission (as much as 50%) may arise from H II regions or cool, diffuse interstellar gas clouds (e.g., Madden et al. 1993).

Whereas [C II] traces both neutral and ionized regions, the higher ionization potential of [N II] (14.53 eV) implies that its fine-structure lines trace only the ionized regime. In particular, the [N II] 205 μm line has a very similar critical density to [C II] 158 μm, meaning that [N II] is useful discriminant of

the origin of the [C II] emission and the [N II]/[C II] ratio is relatively insensitive to gas properties such as density. In addition, the [N II]/[C II] ratio is observed to be proportional to Z_{gas} in Galactic H II regions (e.g., van Zee et al. 1998). At 158 and 205 μm, [C II] and [N II] emission are less susceptible to absorption than other traditional metallicity indicators (Nagao et al. 2012). However, nitrogen is a secondary element in gas enrichment and at low metallicity or at high redshift the gas may be enriched mostly by primary elements (van Zee et al. 1998; Contini et al. 2002), causing N/C to underestimate metallicity. The ability of the ratio to trace metallicity in high-redshift star-forming regions, where the relative extent of [C II] and [N II] emission is unknown, is likely to be limited.

Molecular line emission from ^{12}CO, observed as a series of rotational transitions, is another useful diagnostic for the properties of the ISM. In particular, ^{12}CO(1–0) line intensity is used to estimate the molecular gas mass via a conversion factor α_{CO} that relies on CO tracing the underlying H_2 gas mass (e.g., Solomon & Vanden Bout 2005). The ^{12}CO(1–0) line itself is relatively faint, often forcing an extrapolation from a higher-J transition, using uncertain conversion factors. The full spectral line energy distribution (SLED) has also proven to be a useful diagnostic of the underlying properties of the molecular gas reservoir (such as density and temperature distribution; e.g., Weiss et al. 2005, 2007; Papadopoulos et al. 2010; Danielson et al. 2011). Modern PDR models (Kaufman et al. 1999; Meijerink et al. 2007) account for density, temperature, and time-dependent chemistry to predict emission line ratios for many species, including ^{12}CO, [C II], and [C I]. Comprehensive observation of many lines from a single source may be interpreted using these models to investigate the typical characteristics of the underlying PDR.

At $z \sim 2$, submillimeter galaxies (SMGs) are a significant site of star formation, contributing up to 50% of the cosmic star formation rate (SFR) density (Chapman et al. 2005; Wardlow et al. 2011). However, our understanding of the evolution of galaxies throughout cosmic history is dependent on constraining star formation in the earlier era of stellar mass assembly, with the first major epoch occurring at $z \gtrsim 5$ (e.g., Stark et al. 2010).

The negative slope of the Rayleigh–Jeans tail to the dust component spectral energy distribution (SED) provides a "negative FIR K-correction" as we observe at higher redshifts. Although this tends to aid detection of SMGs at $z > 4$, current instrumentation still only allows detailed observation of the brightest, high-redshift SMGs (e.g., Schinnerer et al. 2008; Riechers et al. 2009, 2013; Coppin et al. 2010; Swinbank et al. 2012; Walter et al. 2012a). However, strong gravitational lensing (by an individual foreground galaxy and/or a massive cluster) increases the signal-to-noise ratio (S/N), providing access to a large suite of emission lines for intrinsically fainter or more distant sources (Baker et al. 2004; Coppin et al. 2007; Danielson et al. 2011; Cox et al. 2011; Weiss et al. 2013). Lensing also increases the apparent angular size of an image, revealing high-redshift sources in incredible sub-kpc spatial resolution (e.g., Swinbank et al. 2009; Jones et al. 2010). Observed source size often correlates with wavelength in lensed sources, so tailored apertures are required for spatially integrated analysis and care must be taken when comparing maps from different spectral windows. We assume that the effect of differential magnification is always negligible, preserving line ratios. This is a good approximation for the bolometric fraction of [C II] and ^{12}CO(1–0), but may introduce some distortion to the CO ladder: e.g., ^{12}CO(6–5)/^{12}CO(1–0) may have uncertainties of up to $\sim$30% due to differential magnification (e.g., Blain 1999; Serjeant 2012).

In Combes et al. (2012, hereafter C12), we presented spatially integrated observations of the bright, lensed SMG HLSJ091828.6+514223 (hereafter HLS0918; R.A. = 09:18:28.6, decl. = +51:42:23). The SMG was discovered in deep FIR imaging from the "*Herschel* Lensing Survey" (HLS; Egami et al. 2010), located at a projected distance of 5″.6 from the X-ray center of the massive cluster A773 ($z = 0.22$). An intermediate-redshift galaxy (at $z = 0.63$) dominates optical imaging at the source position and also contributes $\sim$90% of the lensing effect. C12 reported a source redshift of $z = 5.24$[19] and an estimated total magnification of $\mu \sim 11$. Two kinematic components were identified in the line profiles of multiple ^{12}CO transitions, [N II], [C I], and a water line: a generally brighter, lower-frequency component with water emission, suggesting the presence of an intense FIR radiation field, and a higher-frequency component most prominent in [N II], tentatively interpreted as an ionized gas flow. Recently, Levshakov et al. (2012) utilized the unique set of observed lines to derive a constraint on hypothetical temporal variations in the fundamental physical constants of the universe.

In this paper, we present new [C II] and ^{12}CO(1–0) line emission maps of HLS0918. These are used to characterize the gas properties and morphology of the system in detail. We adopt a new model for the combined cluster/galaxy lens (see Section 3.4), which predicts a total "flux-weighted" magnification factor of $\mu \sim 9$ for HLS0918 and allows us to account for relative amplification of the various components. A detailed description of the lensing constraints and parameters will be presented in F. Boone et al. (in preparation).

The paper is organized as follows. In Section 2, we present the new maps of HLS0918 and summarize existing observations. In Section 3, we analyze the source continuum, derive a self-consistent fit to all of the line profiles, and examine the spatially resolved emission in the maps. Section 4 discusses possible physical interpretation of the results in terms of source-plane morphology and gas properties. Our conclusions are presented in Section 5. Throughout the paper, we use a ΛCDM cosmology with $H_0 = 72$ km s^{-1} Mpc^{-1}, $\Omega_m = 0.27$, and $\Omega_\Lambda = 1-\Omega_m$.

2. OBSERVATIONS

This section describes all observations of HLS0918 employed in the paper: updated reduction of the *Herschel* discovery maps, new, spatially resolved line emission maps of [C II] from the Submillimeter Array (SMA) and ^{12}CO(1–0) from the Very Large Array (VLA), new IRAM 30 m continuum and line observations, additional line profiles and continuum imaging published in C12. We defer description of the line profiles and spatial configuration of the maps until Section 3.

2.1. Herschel and Spitzer

HLS0918 was discovered as an unusually bright "500 μm peaker" source toward the edge of *Herschel*/SPIRE (Pilbratt et al. 2010; Griffin et al. 2010) maps (250, 350, and 500 μm) of A773, observed as part of the HLS (Egami et al. 2010). The SPIRE observations use large-map mode, with a coverage of $\sim$17′ $\times$ 17′. The images were produced via the standard reduction pipeline in HIPE v9.0, the SPIRE Photometer Interactive Analysis package v1.7 and v8.1 calibration product. Note that this is a significant re-reduction since C12, including an

---

[19] We adopt a systemic redshift $z = 5.2430$, as derived from the center of the broad red peak in the high S/N [C II] line. Note that C12 used $z = 5.2429$ from ^{12}CO(6–5).
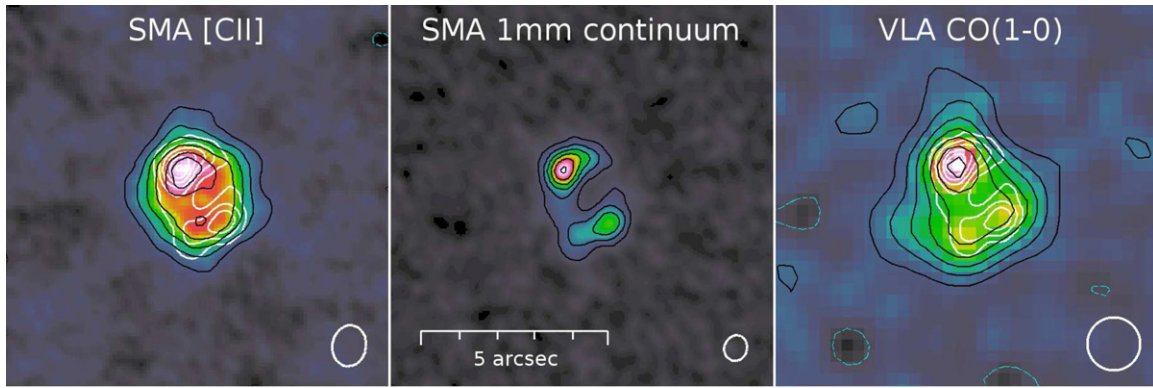
Figure 1. SMA [C II] line emission (left panel), SMA 1 mm (observed-frame) continuum (center), and VLA ^{12}CO(1–0) line emission (right) maps showing a $\sim 10'' \times 10''$ region around HLS0918. North and east are aligned to the top and left, respectively, and the restoring beam size for each map is shown by a white ellipse in the lower right corners. While the color map is "min–max" scaled to accentuate structure, the thick black contours give the $\{2, 4, 6 \ldots\}$, $\{5, 10, 15 \ldots\}$ and $\{1, 2, 3 \ldots\}$ σ confidence levels (left, center, and right panels, respectively). In each panel, thin dashed cyan lines show symmetric negative contours ($\{-2, -4, -6 \ldots\}$, $\{-5, -10, -15 \ldots\}$ and $\{-1, -2, -3 \ldots\}$ σ, respectively). For reference, the morphology of the continuum map is replicated in the other panels as white contours.

(A color version of this figure is available in the online journal.)

improved treatment of the baseline removal (also known as "de-striping"). The SPIRE images are confusion limited ($3\sigma = 17$, 19, 20 mJy; Nguyen et al. 2010) with beam sizes of 18, 25, and $36''$ (250, 350, and 500 μm, respectively).

Herschel/PACS and *Spitzer*/IRAC and MIPS imaging is only available for the core of A773 and does not cover HLS0918 at $r_{\mathrm{cluster}} = 5'.6$.

2.2. Submillimeter Array

SMA imaging data for the [C II] emission line of HLS0918 were obtained in 2011 December (compact array), 2012 February (extended array), and 2012 April (very extended array), reaching a maximum baseline length of ~ 500 m. Observations included ~ 7 hr of on-source integration time per configuration and were conducted in superb weather conditions ($\tau_{225\mathrm{GHz}} \approx 0.05$, phase errors between $10°$ and $30°$ rms). We used the SMA single-polarization 345 GHz receivers, which provide an intermediate frequency coverage of 4–8 GHz, totaling 4 GHz bandwidth per sideband. The receivers were tuned such that the local oscillator frequency was 299.20478 GHz. This ensured that the upper sideband included the entire redshifted [C II] line at $\lambda_{\mathrm{rest}} = 157.74090\,\mu$m, while the lower sideband covered line-free continuum emission from the source at $\lambda_{\mathrm{rest}} \sim 160\,\mu$m ($\lambda_{\mathrm{obs}} \sim 1$ mm).

Calibration of the *uv* visibilities was performed using the Interactive Data Language MIR package. The blazar 3C84 was used as the primary bandpass calibrator and Titan was used for absolute flux calibration. The nearby quasars 0927+390 ($F_{880\,\mu\mathrm{m}} = 0.5$ Jy; $6°$ from the target) and 0920+446 ($F_{880\,\mu\mathrm{m}} = 2.2$ Jy; $15°$ from the target) were used for phase and amplitude gain calibration, respectively.

The Multichannel Image Reconstruction, Image Analysis, and Display software package (Sault et al. 1995) was used to invert the *uv* visibilities and deconvolve the dirty map. Natural weighting was chosen to obtain maximum sensitivity and resulted in an elliptical Gaussian beam with a FWHM of $1''.33 \times 1''.10$ and a position angle of $94°$ east of north. The final integrated (along the frequency axis; $1\sigma \sim 1.1$ mJy beam^{-1}) [C II] emission map is shown in the left panel of Figure 1.

The final 1 mm continuum map was produced from the compact and very extended configurations using AIPS with an IMARG ROBUST factor of 0.0 and a slight down weighting of the

shortest baselines to increase spatial resolution and emphasize structure. This scheme achieves a synthesized beam with $0''.69 \times 0''.60$ FWHM and a sensitivity limit of ~ 0.6 mJy beam^{-1}. The map is displayed in the central panel of Figure 1.

This paper also uses SMA continuum observations of the source obtained at 880 μm (341 GHz) and 1.3 mm (235 GHz) in the compact configuration. The beam sizes for these maps are $2''.1 \times 2''.0$ FWHM and $4''.6 \times 2''.8$ FWHM, respectively, which just resolves the source in the former case. These observations were first presented in C12.

2.3. Jansky Very Large Array

We acquired data using the National Radio Astronomy Observatory VLA in the DnC and C configurations, during 2012 January and April. For approximately 5 hr, we observed two near-contiguous sets of eight contiguous baseband pairs, each comprising 64×2 MHz channels for a total dual-polarization bandwidth of 2048 MHz. We tuned near the ^{12}CO(1–0) transition ($\nu_{\mathrm{rest}} = 115.271203$ GHz; Morton & Noreau 1994) at $\nu_{\mathrm{obs}} = 18.464$ GHz, having offset by 64 MHz to avoid the baseband edge.

Short slots, typically 2 hr long, were scheduled dynamically to ensure excellent phase stability and transparency in the K atmospheric window. The bright ($S_{18.5\,\mathrm{GHz}} \approx 0.8$ Jy) calibration source, J0937+5008, was observed every few minutes to determine accurate complex gain solutions and bandpass corrections. 3C 286 was observed to set the absolute flux scale and the pointing accuracy was checked locally every hour.

The data were reduced and imaged using AIPS following the recipes described by Ivison et al. (2011), although with a number of significant changes: the data were loaded using BDF2AIPS, avoiding any compression, and FRING was used to optimize the delays, in software, based on one minute of data for 3C 286. The basebands were knitted together using the NOIFS task, yielding a *uv* data set with 1024×2 MHz channels centered near the expected frequency of the CO line. The channels were then imaged in groups of four (yielding 130 km s^{-1} velocity resolution), with natural weighting (ROBUST = 5), to form a cube with spatial resolution, $\sim 1''.4$ and a near-circular beam. The map, integrated along the frequency axis ($1\sigma \sim 0.1$ mJy beam^{-1}), is shown in the right panel of Figure 1.

Table 1
HLS0918 Observed Continuum Fluxes

λ_{obs} (mm)	Observatory	S_ν (mJy)
0.25	*Herschel*/SPIRE	96 ± 8
0.35	*Herschel*/SPIRE	179 ± 13
0.50	*Herschel*/SPIRE	212 ± 15
0.88	SMA	125 ± 8
1.0	SMA	103 ± 9
1.3	SMA	55 ± 7
2	IRAM 30 m/EMIR	<21
2	IRAM 30 m/GISMO	9 ± 1
3	IRAM 30 m/EMIR	<2

Approximately one hour of integration was previously obtained using the VLA for the ^{12}CO(2–1) transition at 36.9 GHz, as previously reported in C12.

2.4. IRAM 30 m and PdBI

We present a new 2 mm flux from the Goddard–IRAM Superconducting 2-Millimeter Observer (GISMO; Staguhn et al. 2008) on the IRAM 30 m, observed in 2013 April with an average $\tau_{225\,GHz} \sim 0.3$. The LISSAJOUS_TINY script was used to obtain 30 minutes on source, resulting in a $5' \times 3'$ map with a beam FWHM of $17''.5$ and a source peak S/N of $\sim$10 (reduced via CRUSH; Kovacs 2008). This observation forms part of extensive GISMO follow-up of bright, high-z sources discovered by HLS (IRAM program 221-12; PI: A. Edge) to be fully described in a separate paper. Upper limits on the continuum flux were also previously obtained at 2 and 3 mm using the EMIR heterodyne receivers mounted on the IRAM 30 m, as described in C12.

Our analysis includes a new detection of the ^{12}CO(8–7) transition, observed by EMIR in 2012 mid-December. We tuned EMIR to observe a central frequency of 147.656 GHz and used the wobbler for an efficient subtraction of the sky emission. The atmospheric conditions were good, with 4–6 mm of precipitable water vapor and a system temperature of 130–150 K.

We also take advantage of existing IRAM observations, all presented in C12. These include IRAM 30 m spectra for three additional high-J ^{12}CO transitions ($J_{upper} = 5, 6, 7$), [C I]($^3P_2$–$^3P_1$) 370 μm, H$_2$O$_p$(2, 0, 2–1, 1, 1) 304 μm, and [N II] 205 μm and Plateau de Bure Interferometer (PdBI) data for CO(7–6) and [C I].

3. CONTINUUM AND LINE ANALYSIS

3.1. FIR Continuum and Total Luminosity

SPIRE photometry is derived via a two-dimensional (2D) Gaussian fit to the raw positions of the timestream data (HIPE routine TIMELINESOURCEFITTERTASK), offering a robust measurement unaffected by the pixelization uncertainties inherent in map making. These newly calculated SPIRE fluxes are $\sim$10 mJy larger than quoted in C12. These values, along with the new SMA 1 mm continuum observations and all previous (sub)mm data, are listed in Table 1.

The updated infrared continuum is displayed in Figure 2, overlaid by the best fit Rieke et al. (2009) template shape, allowing for an overall scaling to fit the source peak flux. The best-fit template shape is derived from local LIRGs ($L_{FIR;template} = 10^{11.75} L_\odot$). Integration under this template provides the FIR luminosity of HLS0918, $L_{FIR(8-1000\,\mu m)} = (1.6 \pm 0.1) \times 10^{14} L_\odot$
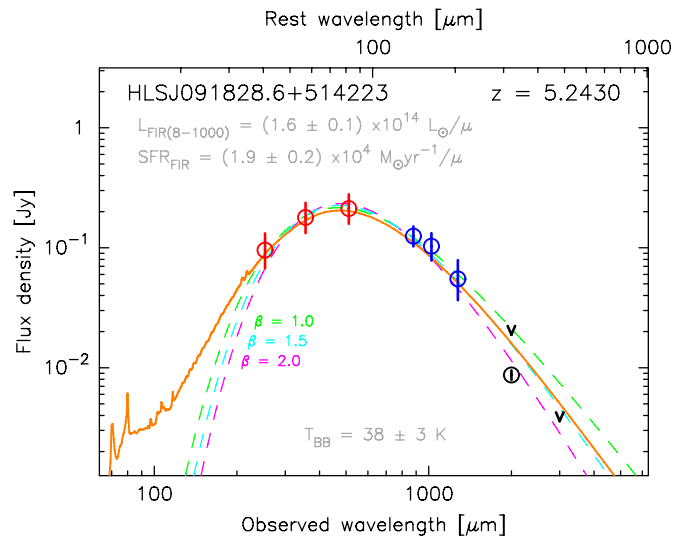
Figure 2. *Herschel*/SPIRE (red), SMA (blue), and IRAM 30 m (black) continuum fluxes. The dashed lines show the best-fit modified blackbody (green, cyan, and magenta for $\beta = 1.0$, 1.5, and 2.0, respectively). For $\beta = 2.0$, which provides the best fit to the millimeter observations, $T_{dust} = 38 \pm 3$ K. The solid (orange) line indicates the best-fit template from Rieke et al. (2009).

(A color version of this figure is available in the online journal.)

μ^{-1}, where μ is the magnification factor (as displayed in the total system properties column of Table 2). Applying the Kennicutt (1998) relation, modified to match the initial mass function (IMF) of Kroupa (2002), as in Rieke et al. (2009),[20] this corresponds to an SFR $= (1.9 \pm 0.2) \times 10^4 \, M_\odot \, yr^{-1} \, \mu^{-1}$. If we instead assume the single power-law Salpeter IMF, as used by Kennicutt (1998), the SFR would be $\sim$50% higher.

We fit a single-temperature graybody to the FIR continuum in order to estimate the characteristic dust temperature (T_{dust}) of the integrated source. We begin by fitting simultaneously for both T_{dust} and the dust emissivity index, β, resulting in $T_{dust} = 48.7 \pm 3.3$ K and $\beta = 1.0 \pm 0.2$.[21] However, the width of the fitted dust peak is driven by the SPIRE fluxes, with less weight given to the single GISMO flux and other IRAM limits, despite these millimeter points preferring a much narrower SED shape. Furthermore, although the above values have the maximum likelihood, a unique solution is not implied by the χ^2 map in T_{dust}–β space, as one would expect from the well-known degeneracy between these parameters (Blain 1999). We therefore proceed with the common practice of assuming a typical value for β, which has the additional benefit of aiding comparisons with previous studies. We calculate the dust temperature assuming, in turn, both $\beta = 1.5$ and 2.0: $T_{dust} = 42.6 \pm 2.9$ K and $T_{dust} = 37.8 \pm 2.6$ K, respectively, assuming that the adopted β has an uncertainty of ± 0.2. The shape of the latter ($\beta = 2.0$) is a better match for the millimeter data (see Figure 2) and agrees with derivations of β for other ULIRGs (e.g., Clements et al. 2010), so we adopt 38 ± 3 K as the canonical characteristic dust temperature of HLS0918.

The dust temperature is lower than those derived for the cores of local ULIRGs from single-temperature fits (e.g., $T_{dust} \approx$ 60–70 K for M82, Arp 220; Panuzzo et al. 2010; Rangwala et al. 2011), but consistent with typical *IRAS* galaxies ($\sim$40 K) and

---

[20] SFR ($M_\odot$ yr^{-1}) $= 0.66 \times$ SFR$_{Kennicutt} = 1.138 \times 10^{-10} L_{FIR} (L_\odot)$.
[21] Following da Cunha et al. (2013), we calculate a negligible dust heating contribution by the cosmic microwave background (CMB; $T_{CMB}^{z=5.24} = 17$ K) of <0.1 K.

Table 2
Derived Properties for HLS0918

Parameter	Unit	Total	Ra	Rb	B	VB	
Relative $L_{1\,mm}$		**1.00 ± 0.04**	0.64 ± 0.03	0.14 ± 0.02	0.21 ± 0.02	0.02 ± 0.01	(1)
T_{dust}	K	**38 ± 3**					(2)
$L_{FIR(8-1000\,\mu m)}$	$\times 10^{12}\,L_\odot\,\mu^{-1}$	**160 ± 10**	104 ± 8	23 ± 4	34 ± 4	2 ± 1	(3)
SFR	$\times 10^3\,M_\odot\,yr^{-1}\,\mu^{-1}$	**19 ± 2**	12 ± 1	2.6 ± 0.5	4.0 ± 0.8	0.3 ± 0.2	(3)
$L_{FIR(42.5-122.5\,\mu m)}$	$\times 10^{12}\,L_\odot\,\mu^{-1}$	**100 ± 6**	65 ± 5	14 ± 2	21 ± 2	2 ± 1	(3)
μ		**8.9 ± 1.9**	9.4 ± 2.0	12.0 ± 2.6	8.4 ± 1.7	4.4 ± 0.9	(4)
$L_{FIR(8-1000\,\mu m),demag}$	$\times 10^{12}\,L_\odot$	**18 ± 4**	11 ± 2	1.9 ± 0.4	4.0 ± 0.8	0.5 ± 0.3	(4)
$L_{[C\,II]}/L_{FIR}$	$\times 10^{-4}$	**8.4 ± 0.5**	5 ± 1	15 ± 5	10 ± 2	73 ± 38	(5)
$L_{CO(1-0)}/L_{FIR}$	$\times 10^{-7}$	**4.3 ± 0.4**	3.1 ± 0.8	8.3 ± 3.7	4.7 ± 1.1	20 ± 20	(5)
M_{gas}	$\times 10^9\,M_\odot$	**≳74 ± 17**	≳31 ± 10	≳15 ± 7	≳18 ± 5	≳10 ± 9	(6)
SFE	$L_\odot\,M_\odot^{-1}$	**≲250 ± 20**	≲360 ± 90	≲130 ± 50	≲230 ± 50	≲60 ± 60	(6)
$L_{[N\,II]}/L_{[C\,II]}$	$\times 10^{-2}$	**5.2 ± 0.6**	3.9 ± 1.6	4.7 ± 2.3	3.9 ± 1.7	12 ± 7	

Notes. Values are uncorrected for magnification μ, unless explicitly stated. Results are presented for both the integrated source (bold "Total" column) and constituent components (Ra, Rb, B, VB; see Section 3.2). Component L_{FIR} assumes relative luminosities derived from the 1 mm continuum map (presented in the first row), given the association between spectral and spatial components identified in Section 3.3.
(1) Relative apparent 1 mm (observed frame) continuum luminosity; Section 3.3.
(2) From a modified blackbody fit; Section 3.1.
(3) From the best-fit Rieke et al. (2009) template; Section 3.1.
(4) From lensing model; Section 3.4.
(5) For a comparison with the literature (e.g., Stacey et al. 2010; De Breuck et al. 2011), we use $L_{FIR(42.5-122.5\,\mu m)}$.
(6) See Section 4.2.

other SMGs observed by *Herschel* (40–50 K; e.g., Danielson et al. 2011; Riechers et al. 2013). Indeed, comparing to the general L_{FIR}–T_{dust} relation (Hwang et al. 2010, Figure 4) and assuming a magnification factor of $\mu \sim 10$, HLS0918 lies within the overlap between the typical ULIRG and SMG regions, as expected. Even accounting for lensing, HLS0918 is an exceptionally bright source ($>10^{13}\,L_\odot$, a "HyLIRG"), yet the shape of the dust continuum resembles a local LIRG, as reported previously for other luminous, high-redshift sources (e.g., Rex et al. 2010).

3.2. Atomic and Molecular Line Emission

In Figure 3, we show the atomic and molecular line emission from HLS0918, which is spatially integrated in the case of the [C II] and ^{12}CO(1–0) maps. The profiles clearly show intensity and kinematic structure, with a similar spectral shape in each line. Here, we describe how we decompose the profiles into a number of spectral components, which can be used to create channel maps in [C II] and ^{12}CO, thus characterizing the source-plane configuration of HLS0918.

First, we examine the high S/N [C II] profile from the SMA to generate an initial model. Two components are immediately obvious: a broad peak ($V \sim 0$ km s^{-1}) and a narrower, blueshifted peak (B; $V \sim -500$ km s^{-1}). We find that the χ^2 of the fit is improved with the addition of a fainter third component at an even greater velocity offset (VB; $V \sim -750$ km s^{-1}). Moreover, the broad component appears double peaked and treating it as two separate entities (Ra, Rb; $V \sim +120$, -130 km s^{-1}) reduces the χ^2 further. Our best-fit model of the line comprises these four Gaussian-profile components.

In order to produce a self-consistent, physically meaningful set of line luminosities, we perform a simultaneous fit to all the observed line profiles described in Section 2—[C II], ^{12}CO ($J_{upper} = 1, 2, 5, 6, 7, 8$), [C I], H$_2O_p$(2, 0, 2–1, 1, 1), and [N II]. The continuum flux is subtracted from each spectrum using a simple linear interpolation from frequencies beyond the emission line ($V < -2000$ km s^{-1}; $V > 1000$ km s^{-1}). The

central velocity and width of each component is only allowed to vary globally (i.e., the same for each line profile), while the peak flux has full freedom for each individual component of every line. This model assumes that for every component, emission in each line originates from the same physical region, which should prove to be a reasonable approximation. The total number of free parameters in the fit is $N = N_C(2 + N_L)$, where N_C is the number of components and N_L is the number of lines. For our current data, $N = 4 \times (2 + 10) = 48$. Uncertainties are calculated via 2000 Monte Carlo simulations in which the observed spectra are randomly fluctuated by their 1σ variance.

The best simultaneous fit, shown overlaying all of the line profiles in Figure 3, gives the following central velocities and widths for each component. Ra: $V = +120 \pm 30$ km s^{-1}, $\Delta V_{FHWM} = 350 \pm 50$ km s^{-1}, Rb: -130 ± 20, 230 ± 30 km s^{-1}, B: -470 ± 10, 160 ± 10 km s^{-1}, and VB: -720 ± 40, 370 ± 170 km s^{-1}. The full fit parameters are presented in Table 3. The advantage of the simultaneous fit is the robust constraint of VB and separation of Ra/Rb, even in spectra with the lowest S/N or coarsest velocity binning. The simultaneous fit is dominated by the high S/N [C II] spectrum. The final luminosity of each component in [C II] is ≲1% different from the best fit to that profile only.

We test whether [C II] is overly dominant, simply forcing the "global" parameters to its own best fit, by repeating the fit with only the moderate S/N spectra: ^{12}CO(2–1), ^{12}CO(6–5), and [N II]. While the parameterization of the B and VB components in this test is essentially identical to the primary result, component Ra is fit by a larger Gaussian profile (and Rb by a correspondingly smaller Gaussian; the Ra/Rb luminosity ratio changes from ∼1–2 to ∼3–4). In the full fit, we find that the Rb/B luminosity ratio is remarkably stable between lines (∼1.2 ± 0.1, excluding H$_2$O, which is undetected for B) and is >1 for all the profiles. In the mid-S/N fit, Rb/B varies widely from 0.1–0.7 (Rb is less luminous than B). Additionally, the red component fit to only mid-S/N lines is a lot less well constrained (twice the χ^2). This test shows that although [C II] does
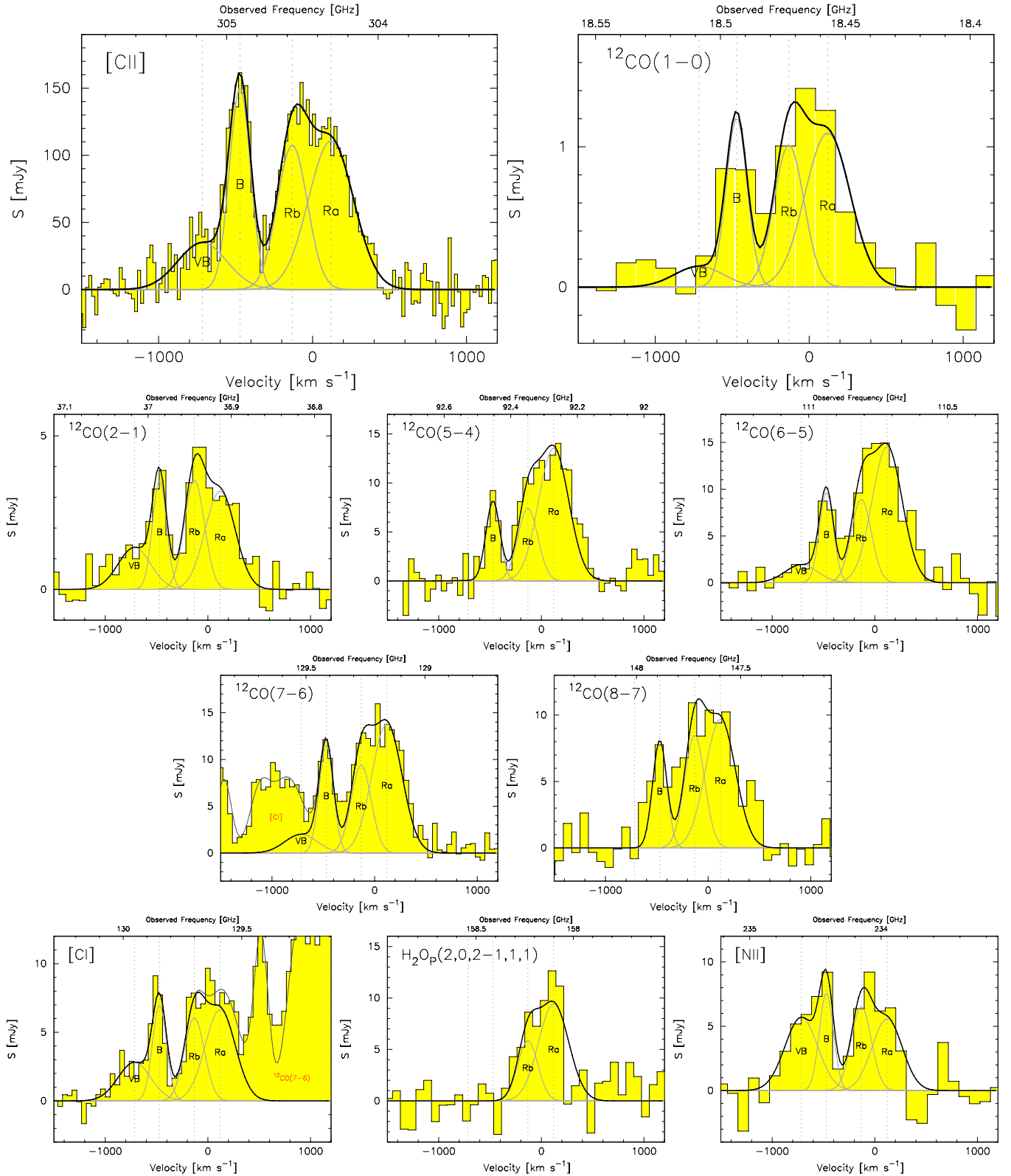
Figure 3. Continuum-subtracted atomic and molecular line profiles: spatially integrated profiles derived from the new [C II] and ^{12}CO(1–0) maps are shown in the top row. The best, fully simultaneous fit by four Gaussian-profile components are overlaid (see Section 3.2 for more details): two red (Ra and Rb; +120 ± 30 and −130 ± 20 km s^{-1}, respectively), a blue (B; −470 ± 10 km s^{-1}), and a "very blue" (VB; −720 ± 40 km s^{-1}). All velocities are relative to the center of the broad [C II] peak ($z = 5.2430$). VB exhibits unusually strong [N II] emission, but no detection for ^{12}CO(5–4) or ^{12}CO(8–7). H$_2$O is only detected for Ra and Rb. Other than this water line, the Rb/B ratio is consistently ∼1.2 ± 0.1.

(A color version of this figure is available in the online journal.)

Table 3
Derived Properties for the Observed Atomic and Molecular Lines; All Values are Uncorrected for Magnification

Line	Component	ν_{obs} (GHz)	S_ν (mJy)	ΔV_{FWHM} (km s^{-1})	V (km s^{-1})	I (Jy km s^{-1})	L ($10^9 L_\odot$)
[C II]	Ra	304.3051	111 ± 9	350 ± 50	+120 ± 30	41 ± 8	33 ± 6
[C II]	Rb	304.5606	108 ± 22	230 ± 30	−130 ± 20	26 ± 7	21 ± 6
[C II]	B	304.9062	151 ± 12	160 ± 10	−470 ± 10	26 ± 4	21 ± 3
[C II]	VB	305.1557	35 ± 8	370 ± 170	−720 ± 40	14 ± 5	11 ± 4
[C II]	**Total**					**107 ± 3**	**85 ± 2**
^{12}CO(1–0)	Ra	18.4567	1.1 ± 0.2	350 ± 50	+120 ± 30	0.40 ± 0.10	0.020 ± 0.005
^{12}CO(1–0)	Rb	18.4722	1.0 ± 0.3	230 ± 30	−130 ± 20	0.25 ± 0.09	0.012 ± 0.005
^{12}CO(1–0)	B	18.4931	1.2 ± 0.2	160 ± 10	−470 ± 10	0.21 ± 0.04	0.010 ± 0.002
^{12}CO(1–0)	VB	18.5083	0.1 ± 0.1	370 ± 170	−720 ± 40	0.06 ± 0.06	0.003 ± 0.003
^{12}CO(1–0)	**Total**					**0.92 ± 0.07**	**0.044 ± 0.003**
^{12}CO(2–1)	Ra	36.9127	3.2 ± 0.4	350 ± 50	+120 ± 30	1.2 ± 0.3	0.11 ± 0.03
^{12}CO(2–1)	Rb	36.9437	3.6 ± 0.7	230 ± 30	−130 ± 20	0.9 ± 0.2	0.09 ± 0.02
^{12}CO(2–1)	B	36.9856	3.5 ± 0.6	160 ± 10	−470 ± 10	0.6 ± 0.1	0.06 ± 0.01
^{12}CO(2–1)	VB	37.0158	1.4 ± 0.3	370 ± 170	−720 ± 40	0.5 ± 0.2	0.05 ± 0.02
^{12}CO(2–1)	**Total**					**3.2 ± 0.2**	**0.31 ± 0.02**
^{12}CO(5–4)	Ra	92.2693	13.5 ± 1.0	350 ± 50	+120 ± 30	5.0 ± 0.8	1.2 ± 0.2
^{12}CO(5–4)	Rb	92.3468	7.4 ± 2.7	230 ± 30	−130 ± 20	1.8 ± 0.8	0.4 ± 0.2
^{12}CO(5–4)	B	92.4516	8.1 ± 1.5	160 ± 10	−470 ± 10	1.4 ± 0.3	0.34 ± 0.06
^{12}CO(5–4)	VB	92.5272		370 ± 170	−720 ± 40	<0.9	<0.2
^{12}CO(5–4)	**Total**					**8.2 ± 0.5**	**2.0 ± 0.1**
^{12}CO(6–5)	Ra	110.7154	14.5 ± 1.5	350 ± 50	+120 ± 30	5.3 ± 1.1	1.6 ± 0.3
^{12}CO(6–5)	Rb	110.8084	8.9 ± 3.4	230 ± 30	−130 ± 20	2.2 ± 1.0	0.6 ± 0.3
^{12}CO(6–5)	B	110.9341	9.7 ± 1.9	160 ± 10	−470 ± 10	1.7 ± 0.3	0.5 ± 0.1
^{12}CO(6–5)	VB	111.0249	1.9 ± 1.3	370 ± 170	−720 ± 40	0.8 ± 0.5	0.2 ± 0.2
^{12}CO(6–5)	**Total**					**10.0 ± 0.7**	**2.9 ± 0.2**
^{12}CO(7–6)	Ra	129.1573	13.8 ± 0.9	350 ± 50	+120 ± 30	5.1 ± 0.8	1.7 ± 0.3
^{12}CO(7–6)	Rb	129.2657	9.4 ± 2.6	230 ± 30	−130 ± 20	2.3 ± 0.8	0.8 ± 0.3
^{12}CO(7–6)	B	129.4124	11.6 ± 1.1	160 ± 10	−470 ± 10	2.0 ± 0.3	0.7 ± 0.1
^{12}CO(7–6)	VB	129.5182	2.0 ± 1.1	370 ± 170	−720 ± 40	0.8 ± 0.4	0.3 ± 0.2
^{12}CO(7–6)	**Total**					**10.2 ± 0.4**	**3.5 ± 0.1**
^{12}CO(8–7)	Ra	147.5943	9.7 ± 1.1	350 ± 50	+120 ± 30	3.6 ± 0.7	1.4 ± 0.3
^{12}CO(8–7)	Rb	147.7182	8.5 ± 2.1	230 ± 30	−130 ± 20	2.1 ± 0.7	0.8 ± 0.3
^{12}CO(8–7)	B	147.8858	8.1 ± 1.5	160 ± 10	−470 ± 10	1.4 ± 0.3	0.5 ± 0.1
^{12}CO(8–7)	VB	148.0068		370 ± 170	−720 ± 40	<1.2	<0.4
^{12}CO(8–7)	**Total**					**7.4 ± 0.5**	**4.6 ± 0.3**
[CI]	Ra	129.5883	6.7 ± 0.9	350 ± 50	+120 ± 30	2.5 ± 0.5	0.8 ± 0.2
[CI]	Rb	129.6971	6.1 ± 1.6	230 ± 30	−130 ± 20	1.5 ± 0.5	0.4 ± 0.1
[CI]	B	129.8443	7.0 ± 1.3	160 ± 10	−470 ± 10	1.2 ± 0.3	0.4 ± 0.1
[CI]	VB	129.9504	2.8 ± 0.8	370 ± 170	−720 ± 40	1.1 ± 0.5	0.4 ± 0.2
[C I]	**Total**					**6.3 ± 0.3**	**2.1 ± 0.1**
H_2O	Ra	158.0979	10 ± 2	350 ± 50	+120 ± 30	3.5 ± 0.9	1.4 ± 0.3
H_2O	Rb	158.2306	6 ± 3	230 ± 30	−130 ± 20	1.4 ± 0.8	0.6 ± 0.3
H_2O	**Total**					**4.9 ± 0.6**	**2.0 ± 0.3**
[N II]	Ra	233.9499	6 ± 2	350 ± 50	+120 ± 30	2.1 ± 0.7	1.3 ± 0.4
[N II]	Rb	234.1464	7 ± 2	230 ± 30	−130 ± 20	1.6 ± 0.7	1.0 ± 0.4
[N II]	B	234.4121	8 ± 3	160 ± 10	−470 ± 10	1.3 ± 0.5	0.8 ± 0.3
[N II]	VB	234.6039	6 ± 2	370 ± 170	−720 ± 40	2.3 ± 0.9	1.4 ± 0.6
[N II]	**Total**					**7.2 ± 0.8**	**4.4 ± 0.5**

Note. Bold rows highlight the source totals.

dominate the solution, the fully simultaneous method provides a more consistent description than individual, or even subset, fits.

There are four further issues to note about the best-fit profiles shown in Figure 3: (1) the best simultaneous fit sets a 3σ upper limit for the undetected VB component of ^{12}CO(5–4) and ^{12}CO(8–7): $I < 0.9$ Jy km s^{-1} ($L < 0.2 \times 10^9 L_\odot$) and

$I < 1.2$ Jy km s^{-1} ($L < 0.9 \times 10^9 L_\odot$), respectively. (2) The [C I] and ^{12}CO(7–6) profiles overlap and consequently the VB component of the latter is buried in the red component of the former. The resulting luminosity for the ^{12}CO(7–6) VB component is not well constrained, which also affects the luminosity of the B component and the [C I] Ra component. However, the best fit produces an Rb/B luminosity ratio of 1.1
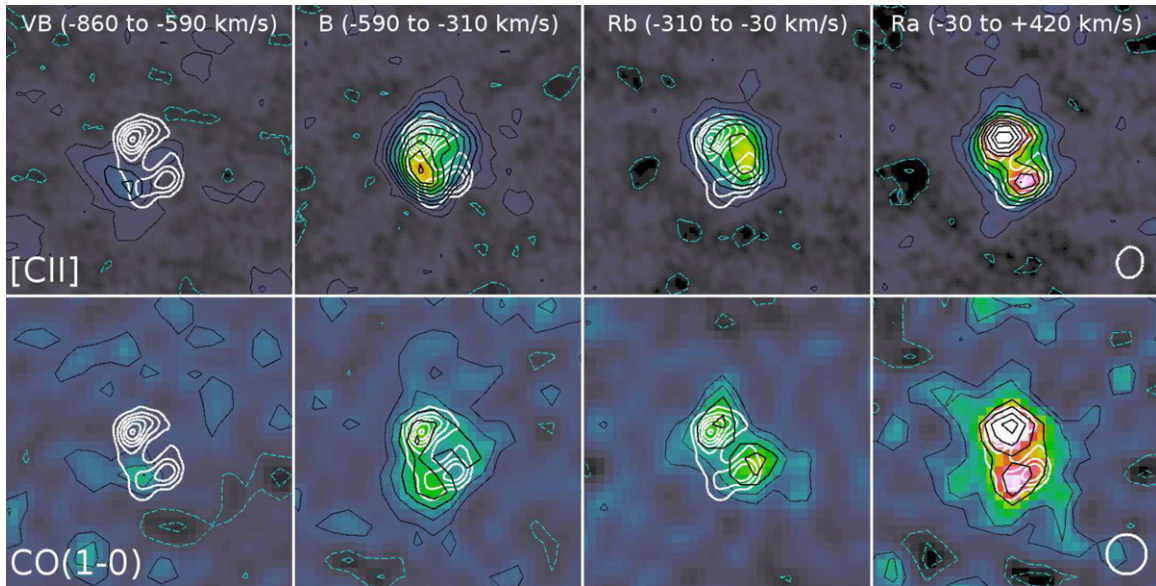
Figure 4. [C II] (upper row) and ^{12}CO(1–0) (lower row) maps showing a $\sim 10'' \times 10''$ region around HLS0918. North and east are aligned to the top and left, respectively, and the restoring beam size for each row is shown by a white ellipse in the lower right corner. Each column displays a unique velocity slice corresponding to the spectral components identified in Section 3.2: -860 to -590 km s^{-1} (VB), -590 to -310 km s^{-1} (B), -310 to -30 km s^{-1} (Rb), and -30 to $+420$ km s^{-1} (Ra). For each row, the color maps are normalized to the peak intensity in the row, to highlight the relative intensity of each component. The black contours give the $\{1, 2, 3 \dots\}\,\sigma$ confidence levels, while dashed cyan contours show the symmetric negative levels. Note that the relation between intensity and S/N for each panel is a function of the velocity bin width. The 1 mm continuum morphology from Figure 1 is shown by white contours on each panel for reference. In [C II] emission, the spectral components correspond extremely well with distinct spatial entities. The division of the red peak into two components is vital to extract the western bridge. For ^{12}CO(1–0), the spatial locations of the Ra, B, and faint VB components agree with [C II] within 1σ, given the beam sizes.

(A color version of this figure is available in the online journal.)

for the ^{12}CO(7–6) line, which is similar to the luminosity ratio in all the other lines, giving us confidence that the simultaneous fit has coped well even in this under-constrained case. (3) The H$_2$O emission line at 304 μm is not detected for the B and VB components. We discuss the interpretation of this line later in the paper. (4) In C12, we interpreted the [N II] profile in terms of a wide, skewed blue peak. The simultaneous fit of a four-component model provides a good fit to the [N II] profile and suggests that the unusual blue peak actually results from a strong VB component. The relative luminosity of [C II] and [N II] in the Ra, Rb, and B components is approximately equal, whereas VB shows significantly enhanced [N II]/[C II]. We explore this ratio further in Section 4.4.

3.3. Spatially Resolved Emission

We turn our attention to the spatially resolved maps obtained using the SMA and the VLA, attempting to connect morphological structure to the spectral components identified in Section 3.2. The SMA 1 mm continuum map (Figure 1) has the smallest beam and reveals two bright components, separated by approximately $2''$ and roughly orientated north/south. The brighter northern component particularly appears to be extended, while the two are linked by a low surface brightness bridge to the east. The flux ratio of the north/south components in the 1 mm continuum is ~ 1.7.

The SMA map of [C II] 158 μm and the VLA map for the ^{12}CO(1–0) transition both display a similar morphology to the 1 mm continuum map (Figure 1), with bright north and south components clearly visible. However, both integrated line maps show a larger fraction of flux originating from between the north and south peaks, particularly to the west.

The [C II] and ^{12}CO(1–0) data cubes have a high enough S/N to allow for subdivision into velocity bins. We choose

bins corresponding to the spectral components identified in Section 3.2. Specifically, bin boundaries are taken at velocities where overlapping components have equal contribution to the total flux (-860, -590, -310, -30, and $+420$ km s^{-1}). Figure 4 displays the resulting maps. Concentrating first on the high S/N [C II] data (upper row), the spectral components are clearly located in distinct locations on the sky. Ra corresponds to the bright north and south peaks visible in the 1 mm continuum map. The Rb and B appear as two arcs, to the west and east, respectively, with the latter aligned to the bridge identified in the continuum map. Division of the broad "red" spectral peak into Ra and Rb components is essential to extract the western bridge. The faint VB spectral component appears as a faint source to the southeast of the continuum flux.

The ^{12}CO(1–0) data have a lower S/N and a poorer spatial resolution than [C II], as highlighted by the significance (σ) contours in Figure 4. Despite these limitations, we can identify many similarities to the [C II] maps. The spatial location of the two Ra peaks are within 1σ (given the ^{12}CO(1–0) beam size) of the corresponding [C II] peaks. Similarly, the ^{12}CO(1–0) component B is dominated by the eastern bridge and VB is entirely located to the southeast (albeit only at $\sim 3\sigma$). In contrast, the Rb component is not in such good agreement, with the western bridge seen in the [C II] emission replaced by two peaks similar to the Ra component. One interpretation is that the [C II] and ^{12}CO(1–0) emission in Rb originates from very different locations. However, the similarity of the locations of Rb to Ra in the CO line instead suggests that the velocity width of the Ra component is larger in ^{12}CO(1–0) than [C II], leaking into the adjacent bin and drowning out the Rb flux. Unfortunately, further investigation, such as constraining just the CO line profile fit with different parameter values, is hampered by the poor S/N of the VLA data, although we do note that the spectral peak for Ra in ^{12}CO(1–0) is skewed toward lower velocities
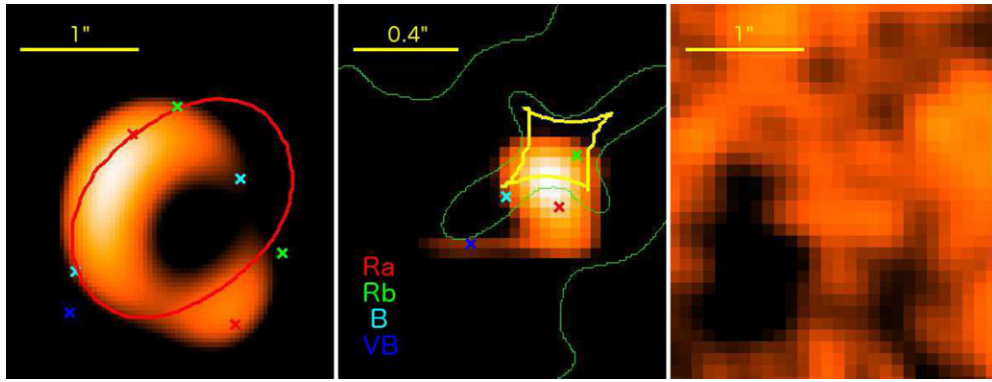
Figure 5. Lensing model for HLS0918 (to be presented in detail in F. Boone et al., in preparation). Left panel: sum of the flux in the four components for the model of HLS0918, after passing through the model lens and convolving with the SMA beam. The critical line is marked in red, while the crosses refer to the local maxima of each component in the image plane before convolution (i.e., directly through the lens). Central panel: sum of the four components in the source plane (without SMA beam convolution). The caustic line is marked in yellow, while the crosses mark the position of each component peak. Magnifications of $\mu = 2, 5$ are shown by the green contours. $\mu = 10$ lies very close to the caustic. Right panel: residual map of the total model flux in the image plane subtracted from the observation.
(A color version of this figure is available in the online journal.)

than in [C II] (see Figure 3). Such a difference in line width could be caused by the emission originating from different radii within the same star-forming cloud, but such an offset would be negligible compared with the beam size of our maps. Generally, the same structure appears in each velocity range for both [C II] and $^{12}CO(1–0)$, verifying that they are not an artifact of instrumentation or unique to a particular line.

Finally, we estimate the apparent FIR luminosity of each component. We use the association between spectral and spatial components to derive the relative luminosity of each in the 1 mm continuum map. Assuming that the 1 mm continuum reflects the morphology of the continuum in general (and the shape of the dust SED in each component is comparable), we can then estimate L_{FIR} for each component. We approximate each of the northern and southern components in the 1 mm map with a 2D Gaussian profile. Subtracting these from the map results in a residual image containing the spatially separated flux of the east and west bridges. We allocate flux to these pixel-by-pixel, using a line bisecting the gap. Two-thirds of the continuum flux originates from the northern and southern components combined (spectral component Ra). The western and eastern regions (Rb and B, respectively) contribute ~10% and 20% of the total flux, respectively. We estimate the flux attributed to the VB component by assuming that the eastern component is a scaled version of the western source (VB is the residual from subtracting a rotated and scaled western component from the east). The VB component is attributed to ~1.5% of the total flux. This allocation method accounts for $101\% \pm 4\%$ of the integrated continuum flux (first row, Table 2), which suggests that the continuum morphology is well modeled by the four components of the line emission.

The first row of Table 2 presents the relative apparent continuum luminosities. L_{FIR} and SFR for each separate component are derived from these fractions and are also shown in Table 2 (without correcting for magnification).

3.4. Lensing Model

Derivation of the absolute luminosity, along with other source-plane characteristics such as the true morphology, requires a well-constrained model of the magnification and distortion due to lensing. For HLS0918, the lens model has to combine the effect of both A773 ($z = 0.22$) and the foreground galaxy at $z = 0.63$. The large distance from the center of A773 (5′.6)

means that the cluster lens effect is secondary (a ~10% contribution). The best possible lens model is derived using LENSTOOL (Jullo et al. 2007), via constraints obtained from both the SMA data described in this paper and additional observations from the PdBI, to be presented in F. Boone et al. (in preparation). Comprehensive, quantitative details of the observed constraints and parameters for the lens model, including an in-depth analysis of differential lensing enabled by the higher spatial resolution PdBI imaging, will be given in Boone et al.

For the purposes of this paper, we only attempt to reconstruct the source-plane configuration of HLS0918 from the four components identified in the SMA [C II] and 1 mm continuum maps. Figure 5 shows the derived source-plane configuration alongside the predicted SMA (image-plane) observation for HLS0918, given the best-fit lens model and the residual map of the model flux in the image plane subtracted from the observation. We find that the four components described in the previous section (plus two faint images of components Rb and B, which are not directly identified in the observed maps) originate from four source-plane regions separated by ≲4 kpc (equivalent to ≲0′.5 on the sky without a lens).

The bright northern and southern sources are indeed two images of the same region (together magnified by $\mu_{Ra} = 9.4 \pm 2.0$), as suggested by their identical velocity offset in the line profile. The vast majority of the source-plane flux is from Ra, which is located approximately half inside and half outside the caustic (although the peak is located outside; Figure 5). In the image plane, the total flux is dominated by the part of component Ra that is crossing the caustic. The model indicates that both Rb and B also cross the caustic, producing double images with amplification factors of $\mu_{Rb} = 12.0 \pm 2.6$ and $\mu_B = 8.4 \pm 1.7$, respectively. In the observed SMA [C II] maps for the individual components (Figure 4), the two images of Rb are not quite spatially resolved, while the western image of component B is only marginally visible: the Rb/Ra and B/Ra flux ratios are low, so the double image of Ra dominates in the frequency-integrated image-plane maps. The VB component originates from a region entirely outside of the caustic and undergoes a lower magnification (although still $\mu_{VB} = 4.4 \pm 0.9$, as shown by the magnification contours in the central panel of Figure 5), resulting in a single image. The total ("flux-weighted") magnification of the full source HLS0918 is $\mu_{total} = 8.9 \pm 1.9$. All of these magnification factors are listed in Table 2.
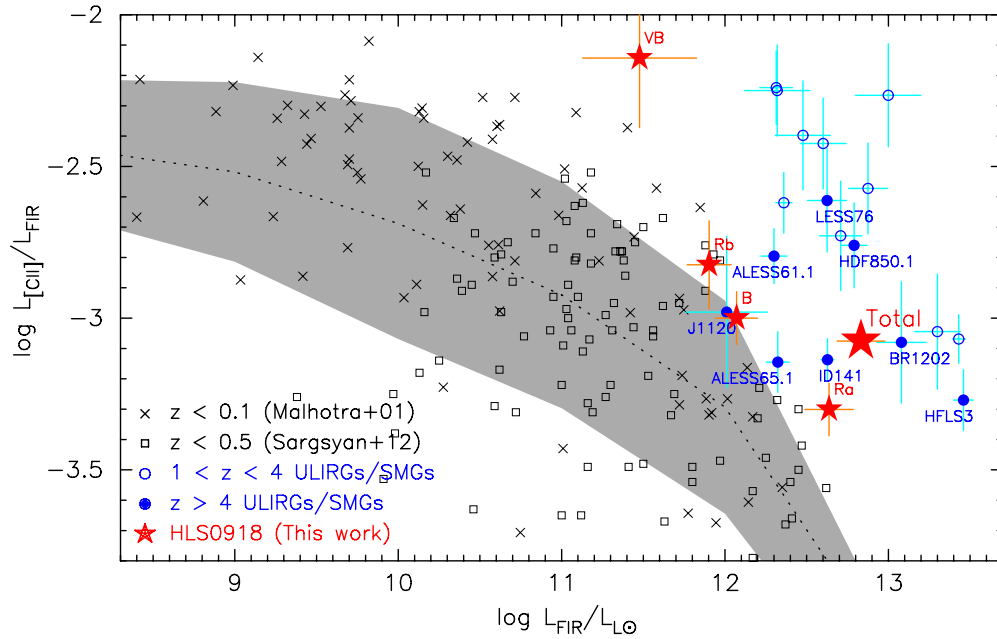
Figure 6. $L_{[C\,II]}/L_{FIR}$ vs. L_{FIR}. HLS0918 (large red star) and constituent components (smaller red stars) assume magnifications as shown in Table 2. High-redshift ($z > 4$) ULIRGs/SMGs (filled blue circles; labeled with source name) from Cox et al. (2011), De Breuck et al. (2011), Swinbank et al. (2012), Venemans et al. (2012), Wagg et al. (2012), Walter et al. (2012b), and Riechers et al. (2013). $1 < z < 4$ ULIRGs/SMGs (open blue circles) are from Stacey et al. (2010) and Valtchanov et al. (2011). Low-redshift star-forming galaxies based on *Infrared Space Observatory* data from Malhotra et al. (2001) and *Herschel*/PACS data from Sargsyan et al. (2012) are shown as crosses and open squares, respectively. For the local data, we calculate the median (dotted line) and scatter (1σ = gray shaded area). HLS0918 is located in the same region as the other high-luminosity, high-redshift sources, which exhibit $L_{[C\,II]}$ approximately an order of magnitude larger than local galaxies with similar FIR luminosity. The individual components of HLS0918 show an excess of 2–3.

(A color version of this figure is available in the online journal.)

Combining the magnification factors with the apparent luminosities derived in the previous section, we compute the absolute FIR luminosity: $L_{FIR,demag} = (1.8 \pm 0.4) \times 10^{13}\,L_\odot$. Of the components, Ra is by far the brightest with $L_{FIR,Ra,demag} = (1.1 \pm 0.2) \times 10^{13}\,L_\odot$. Rb and B have similar luminosities to each other: $L_{FIR,Rb,demag} = (1.9 \pm 0.4) \times 10^{12}$ and $L_{FIR,B,demag} = (4.0 \pm 0.8) \times 10^{12}\,L_\odot$. The lower amplification of VB ($L_{FIR,VB,demag} = (4.5 \pm 2.5) \times 10^{11}\,L_\odot$) means that the source-plane luminosity ratio between that component and Rb or B is not as large as in the image plane.

Magnification is a strong function of source-plane position relative to the caustic line. If the emission regions are significantly more compact than the SMA observations can resolve, then these components may not extend as far beyond the caustic as currently assumed. We caution that the true magnification could be higher than estimated. The total magnification could be as large as $\mu_{total} \sim 15$. Similarly, the data presented in this paper do not allow us to constrain differential magnification, caused by size differences in the emission regions of different lines. We do, however, reiterate that the [C II] and ^{12}CO(1–0) maps presented here are consistent (within 1σ in flux and the VLA beam size) with a scenario in which all line emission from a particular component originates from a single region. A source-plane reconstruction utilizing all of the higher spatial resolution PdBI data may better constrain the size of the components, estimate the effect of differential magnification, and determine the total amplification (F. Boone et al., in preparation).

4. DISCUSSION

Emission line ratios provide a powerful probe of the physical conditions within the photon-dominated regions of the ISM. Together with the lens model predictions of the source-plane configuration, we can characterize the nature of HLS0918

in great detail. We begin with the simple luminosity ratios $L_{[C\,II]}/L_{FIR}$ and $L_{CO(1-0)}/L_{FIR}$, which provide an easy way to connect various dust, gas, and ISM properties in each component. To form a more complete characterization of the star-forming gas, we then move to the interpretation of multiple molecular and atomic lines via complex PDR models. We also re-examine the [C I], water, and [N II] emission reported for HLS0918 in C12. Together, these three lines can help explore phenomena vital to understanding the properties of HLS0918 in particular, but also the evolution of the high-redshift galaxy population in general: gas metallicity and feedback mechanisms via AGNs and outflowing material.

Throughout this discussion, differential magnification is considered to have a negligible effect. Generally, this is a good approximation for bolometric fractions of [C II] and ^{12}CO(1–0) and the current data provide no evidence for significant differences in the spatial location of the components in those two lines (Figure 4). However, the assumption is almost certainly poor for ratios within the ^{12}CO SLED (Serjeant 2012) and hence we are careful to draw conclusions from order-of-magnitude estimates only. We facilitate comparison with previous studies by adopting the definition $L_{FIR(42.5-122.5\,\mu m)}$ (e.g., Stacey et al. 2010; De Breuck et al. 2011), rather than $L_{FIR(8-1000\,\mu m)}$, for both $L_{[C\,II]}/L_{FIR}$ and $L_{CO(1-0)}/L_{FIR}$, as noted in Table 2.

4.1. $L_{[C\,II]}/L_{FIR}$

$L_{[C\,II]}/L_{FIR}$ is a sensitive probe of physical conditions within the ISM. High-z sources often exhibit ratios larger by an order of magnitude or more than local star-forming galaxies of similar FIR luminosity (e.g., Stacey et al. 2010; Swinbank et al. 2012), which is usually attributed to large, extended [C II] reservoirs.

Figure 6 displays this ratio as a function of FIR luminosity, correcting for the effect of magnification. The integrated source

has $L_{[C\,II]}/L_{FIR} = (8.4 \pm 0.5) \times 10^{-4}$, which lies significantly above nearby ULIRGs and is consistent with other star-forming galaxies at $z > 4$. Generally, these galaxies exhibit a smaller offset from the local ULIRG population than those at the epoch of peak star formation ($z \sim 2$), although selection bias and small number statistics are unaccounted for. Component Ra exhibits a lower ratio [$(5 \pm 1) \times 10^{-4}$], while components Rb and B are similar to each other [(1.5 ± 0.5) and $(1.0 \pm 0.2) \times 10^{-3}$] and larger than Ra. Individually, components Ra, Rb, and B are much closer to the locus of local star-forming galaxies than the integrated source: individual high-z clumps may not be as different from local star formation as the integrated galaxies suggest. VB has stronger [C II] emission given its FIR luminosity [$(7 \pm 4) \times 10^{-3}$], which is more similar to much lower FIR luminosity systems in the local universe. This may indicate that VB lacks an extended [C II] reservoir.

4.2. Gas Mass and Star Formation Efficiency ($L_{CO(1-0)}/L_{FIR}$)

The stability and abundance of CO molecules in interstellar clouds (predominantly composed of H_2) implies that the ubiquitous emission from CO rotational transitions is an important tracer of total gas mass. As L_{FIR} quantifies star formation in dusty systems, the $L_{CO(1-0)}/L_{FIR}$ ratio is therefore a useful diagnostic for the star formation efficiency (SFE). The VLA $^{12}CO(1-0)$ observation of HLS0918 is particularly important, removing the need to extrapolate $L_{CO(1-0)}$ from higher-J transitions.

For the integrated source, $L_{CO(1-0)}/L_{FIR} = (4.3 \pm 0.4) \times 10^{-7}$, which sits toward the upper envelope (i.e., most efficient) of $z \sim 2$–3 literature values (e.g., De Breuck et al. 2011), but is similar to the ratio for the $z = 2.3$ "Eyelash" galaxy (SMMJ2135) reported to have $L_{CO(1-0)}/L_{FIR} = 5 \times 10^{-7}$ (Danielson et al. 2011). SMGs at $z > 5$ show a similar spread in this ratio as their $z \sim 2$–3 counterparts, e.g., HDF850.1 ($z = 5.2$; Walter et al. 2012b) and HFLS3 ($z = 6.3$; Riechers et al. 2013) with $L_{CO(1-0)}/L_{FIR} \sim 1$–$2 \times 10^{-7}$. Components Ra and B exhibit comparable $L_{CO(1-0)}/L_{FIR}$ to each other, resembling more the higher SFEs of intermediate redshift ($z \sim 1$–2) ULIRGs (e.g., Combes et al. 2011, 2013). Component VB has an extremely elevated $L_{CO(1-0)}/L_{FIR}$, although we note the large error bar that suggests the component is on the limit of detection in the $^{12}CO(1-0)$ profile.

We quantify the total gas mass from the lensing-corrected ^{12}CO line luminosity[22] via the basic relation

$$M_{H_2} = \alpha_{CO} L'_{CO(1-0),unlensed}, \tag{1}$$

where M_{H_2} ($M_\odot$) is defined to include helium such that $M_{H_2} = M_{gas}$ (Solomon & Vanden Bout 2005) and α_{CO} ($M_\odot$ (K km s^{-1} pc^2)$^{-1}$) is the conversion factor. Assuming that the $^{12}CO(1-0)$ emission is optically thin and the environment is solar metallicity, we can estimate a lower limit for α_{CO} and hence total gas mass. Following Ivison et al. (2010a) and Danielson et al. (2011):

$$\alpha_{CO} = 0.08 \left\{ \frac{g_1}{Z} e^{-T_0/T_k} \left(\frac{J(T_k) - J(T^z_{CMB})}{J(T_k)} \right) \right\}^{-1}$$
$$\times \left(\frac{[^{12}CO/H_2]}{10^{-4}} \right)^{-1}, \tag{2}$$

---

[22] CO line luminosity (in K km s^{-1} pc^2) via $L'_{CO(1-0)} = 3.25 \times 10^7 I_{CO} \nu_{obs}^{-2} D_L^2 (1+z)^{-3}$ with integrated luminosity I_{CO} in Jy km s^{-1}, ν_{obs} in GHz, and luminosity distance D_L in Mpc.

where $g_1 = 3$ (the degeneracy of level $n = 1$), the partition function $Z \sim 2(T_k/T_0)$, $T_0 = 5.5$ K, $J(T) = T_0(e^{T_0/T} - 1)^{-1}$, and $[^{12}CO/H_2] \sim 10^{-4}$ (based on Mk231; Bryant & Scoville 1996). We adopt a lower limit on gas temperature $T_k > 40$ K, as gas couples well to warm dust in a dense star-forming system (Narayanan et al. 2011). For HLS0918 at $z = 5.2430$, $T^z_{CMB} = (1+z)T^{z=0}_{CMB} \sim 17$ K and we therefore estimate $\alpha_{CO} \gtrsim 0.7$, which is consistent with the value for a smoothly distributed, largely molecular ISM, as observed in local ULIRGs ($\alpha_{CO} \sim 0.8$; e.g., Solomon & Vanden Bout 2005).

The lower limit on the total gas mass for HLS0918 is $M_{gas} \gtrsim (74 \pm 17) \times 10^9 \, M_\odot$. Assuming that α_{CO} is the same for all components, Ra contains almost half the mass, $M_{gas} \gtrsim (31 \pm 10) \times 10^9 \, M_\odot$, while the remainder is distributed roughly equally among Rb, B, and VB.

We can now use the absolute gas mass to calculate the SFE in physical units: SFE (in $L_\odot \, M_\odot^{-1}$) = L_{FIR}/M_{gas} (Greve et al. 2005). HLS0918 has a maximum SFE $\lesssim 250 \pm 20 \, L_\odot \, M_\odot^{-1}$, which does not conflict with the absolute limit due to radiation pressure derived by Scoville (2004), SFE$_{max}$ = $500 \, L_\odot \, M_\odot^{-1}$. Individually, components Ra, Rb, and B have SFEs in the range 130–360 $L_\odot \, M_\odot^{-1}$. Component VB exhibits a lower SFE $\lesssim 60 \pm 60 \, L_\odot \, M_\odot^{-1}$. Although the apparent continuum flux of VB is significantly lower than the other components, the total molecular gas mass is similar to that of Rb and B. This is due to both a smaller amplification, effectively decreasing the overall relative luminosity of VB, and an intrinsically lower SFE, which results in an enhanced $L_{CO(1-0)}/L_{FIR}$. HLS0918 corresponds well with the general population of high-redshift SMGs, averaging $\sim 260 \, L_\odot \, M_\odot^{-1}$ (e.g., Riechers et al. 2010; Danielson et al. 2011; Thomson et al. 2012).

Finally, we examine the Kennicutt–Schmidt (KS) relation, a power law linking the surface densities of SFR and molecular gas (Σ_{SFR} and Σ_{gas}). The trend is near-linear for a wide range of gas densities ($\Sigma_{gas} \gtrsim 0.1 \, M_\odot$ pc^{-2}) and at all observed redshifts (e.g., Kennicutt 1998; Genzel et al. 2010; Decarli et al. 2012; Tacconi et al. 2013), suggesting that the mode of star formation is relatively consistent throughout time. We estimate the mean surface densities for HLS0918 from the resolved emission in the SMA 1 mm continuum and VLA $^{12}CO(1-0)$ maps, which can be converted to SFR and gas mass, respectively, using the prescriptions described in earlier sections. HLS0918 is located at the upper envelope of the general KS relation (Figure 7), along with other bright, high-z sources such as GN20 at $z = 4.05$ (Carilli et al. 2010). $\Sigma_{gas}/\Sigma_{SFR}$ is a crude estimate of the consumption timescale, with the estimate for the $1 < z < 4$ star-forming population located between ~ 50 Myr and 5 Gyr, with a mean ~ 800 Myr. HLS0918, along with GN20 and HXMM01 (Fu et al. 2013; $z = 2.3$), shows a shorter gas consumption timescale than this (10–50 Myr). However, Σ_{gas} is derived from $^{12}CO(J > 1)$ for the $1 < z < 4$ galaxies in Figure 7, which may overestimate the density compared with $^{12}CO(1-0)$. The paucity of lower redshift galaxies with either $^{12}CO(1-0)$ observations or such large SFR surface densities means that a direct comparison is difficult: are these bright examples offset due to an intrinsic difference in the mode of star formation or is this a selection effect whereby we are only probing the upper edge of the population?

We can examine the resolved KS relation for HLS0918. Although we can separate the individual components, we do not know the spatial extent of each clump and cannot directly determine the surface densities. Instead, we grid the spatial data
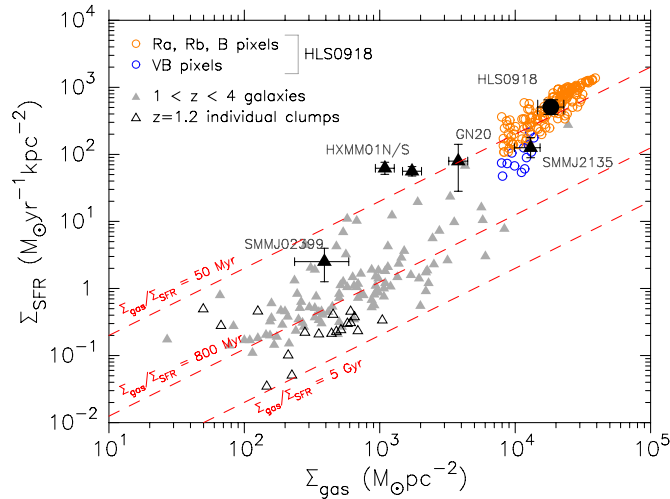
Figure 7. Kennicutt–Schmidt relation: SFR and total molecular gas surface densities (Σ_{SFR} vs. Σ_{gas}). The mean surface densities for HLS0918 are shown by black circles. Open circles display the per-pixel values: pixels dominated by flux from component VB (highlighted in blue) are located beyond the general locus of values for HLS0918. Note that the VB pixels are all correlated in Σ_{SFR}, as the component is not resolved in the ^{12}CO(1–0) beam. Filled triangles show additional star-forming galaxies ($z \sim 1$–4; Genzel et al. 2010; Tacconi et al. 2013), with well-known bright sources labeled (Carilli et al. 2010; Ivison et al. 2010a; Danielson et al. 2011; Fu et al. 2013). Open triangles display individual star-forming clumps within four massive galaxies at $z = 1.2$ (Freundlich et al. 2013). The red dashed lines indicate constant gas consumption timescales for the star-forming regions of 50 Myr, 800 Myr, and 5 Gyr. The $1 < z < 4$ star-forming population exhibits a mean of ~800 Myr, while HLS0918 lies above the upper extreme with a consumption timescale <50 Myr.

(A color version of this figure is available in the online journal.)

to calculate the mean surface densities for different regions of HLS0918 (in the image plane). We adopt the ^{12}CO(1–0) map pixel size ($0''.3 \times 0''.3$) as the most convenient binning regime. The continuum map is smoothed to the ^{12}CO(1–0) beam and re-binned, to give SFR surface density in bins exactly matched to the gas surface densities. The densities are corrected for mean component amplifications, but we do not account for pixel-scale magnification gradients. Gravitational lensing conserves surface brightness. Figure 7 shows that the binned points form a generally elliptical locus about the mean value. A small fraction of pixels are offset from the main population (at lower SFR surface density for a given Σ_{gas}). Although it is hard to distinguish the effect of components Rb and B from the dominant Ra, component VB is more isolated spatially. We find that the offset pixels are from the region coincident with VB, presenting further visual evidence that VB has an intrinsically lower SFE than the rest of HLS0918. However, VB is certainly not atypical compared with other star-forming sources, with the bright lensed galaxy SMMJ2135 (Danielson et al. 2011) located in the same region of the KS plot.

4.3. Physical Properties of the PDR

For a more detailed exploration of the ISM properties, we now employ the solar metallicity PDR models of Kaufman et al. (1999, hereafter K99) and the higher metallicity (twice solar) models from Meijerink et al. (2007, hereafter M07). Both models parameterize PDR characteristics in terms of atomic gas density (n in cm^{-3}) and incident FUV flux from young massive stars (G_0 in Habing fields). K99 present a simple model where the assumed geometry is of a cloud illuminated on one side. A more realistic model would assume illumination of the

cloud on all sides and therefore optically thick emission is detected only from the near side of the cloud and optically thin emission is detected from both the near and far sides, affecting the observed line ratios. Corrections may be applied to account for this, but we choose not to here. Instead, we also compare with a more geometrically complicated model from M07 that involves two or more clouds with differing densities and incident radiation fields. In both models, we assume that all the observed emission lines in a single component are coming from the same gas, which is a vast oversimplification and, again, we do not account for differential magnification. We do, however, correct the observed line luminosities to account for the contribution from gas excitation by the warmer CMB at $z > 5$ ($T_{\mathrm{CMB}}^{z=5.24} = 17$ K). The appropriate correction for each line is estimated via the RADEX code (van der Tak et al. 2007), assuming $T_k = 40$ K. Corrections are small, but not negligible: averaged over likely gas densities ($\log n \sim 2$–6), we estimate ~40% for ^{12}CO(1–0), 15% for high-J CO transitions, and 4% for [C II], which agrees well with da Cunha et al. (2013, Figure 10). We discuss these corrections in more detail later in this section. Overall, the simplifications in modeling restrict our discussion to order-of-magnitude estimates of the characteristic properties.

We begin with the simplest analysis: direct comparison of $L_{\mathrm{[C\,II]}}/L_{\mathrm{FIR}}$ and $L_{\mathrm{CO(1-0)}}/L_{\mathrm{FIR}}$ (Stacey et al. 1991, 2010; De Breuck et al. 2011). Figure 8 presents the location of HLS0918 and the constituent components on this diagnostic plot, with typical PDR characteristics indicated by a simple inversion of the K99 model. These contours assume that the [C II], ^{12}CO(1–0), and FIR emission is PDR-driven, as the CMB heating effect at $z = 0$ (where $T_{\mathrm{CMB}}^{z=0} = 2.73$ K) is negligible. For HLS0918, we plot both the observed ratios and those including the correction for CMB heating at $z = 5.2$, as described above (~0.2 dex shift). The correction tends toward both lower gas densities and lower G_0. The corrections and uncertainties ensure that a direct estimate of n and G_0 is not meaningful, but we can compare the general location of the HLS0918 components with other observed galaxy populations. The integrated emission from HLS0918 is similar to local ULIRGs and less than 0.5 dex from three well-studied, high-redshift sources: the SMG HFLS3 ($z = 6.34$; Riechers et al. 2013), the quasar host galaxy BRI1335–0417 ($z = 4.41$; Riechers et al. 2008), and BRI1202–0725N, the SMG component of a quasar/SMG merger at $z = 4.7$, which cannot be deblended from its companion at some wavelengths (Momjian et al. 2005; Salomé et al. 2012). In contrast, two other well-studied high-z SMGs, SMMJ2135 ($z = 2.3$; Swinbank et al. 2010; Ivison et al. 2010b) and LESSJ0332 ($z = 4.76$; De Breuck et al. 2011), are more than half a magnitude larger in $L_{\mathrm{[C\,II]}}/L_{\mathrm{FIR}}$, which is interpreted as an atomic gas density more than a magnitude lower than that of HLS0918.

Component Ra exhibits the highest gas density and strongest incident FUV field, which may indicate a very intense nuclear starburst or the presence of an AGN. The latter explanation is perhaps supported by the similarity of Ra in these luminosity ratios to two known, high-z quasar hosts. Figure 8 shows that components Rb and B have lower densities and generally weaker FUV radiation fields than Ra, suggesting a mode of star formation more analogous to local LIRGs, i.e., star formation occurring on larger physical scales rather than in a compact region. This suggests that the star formation prescriptions derived from the brightest galaxies in the local universe may not be applicable to the extreme star-forming SMGs, despite both exhibiting similar (ULIRG) luminosities. Finally, the luminosity
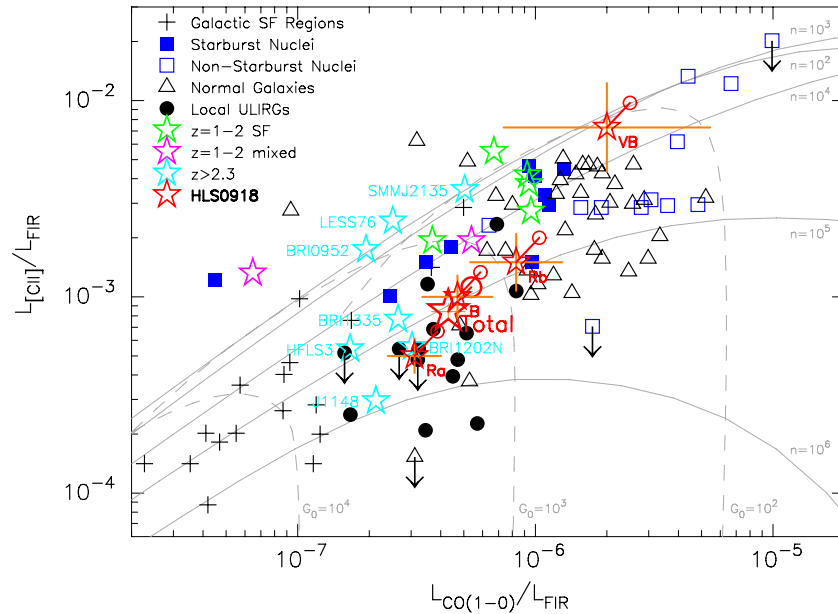
Figure 8. $L_{[C\,II]}/L_{FIR}$ vs. $L_{CO(1-0)}/L_{FIR}$ diagnostic plot (adapted from De Breuck et al. 2011). HLS0918 (labeled red stars; integrated and spectral components plotted separately) is compared with a variety of local and high-redshift sources. For consistency with the high-redshift sources taken from the literature, we plot the HLS0918 ratios uncorrected for CMB heating effects (labeled red stars). The gray lines represent the solar metallicity PDR models with varying gas density (n) and FUV field strength (G_0) from K99. However, these models are for the CMB temperature at $z = 0$ and we note that at $z > 4$ the effect of the warmer CMB becomes increasingly more significant. Thus, for HLS0918, we also artificially correct for $T_{CMB}^{z=5.24} = 17$ K, which increases the ratios by ∼0.2 dex (open red circles, linked by red lines to the corresponding uncorrected point) and systematically moves the points toward lower n and G_0 (see the text for details). Regardless of these corrections, components Ra, Rb, and B appear similar to local ULIRGs and Ra also most resembles high-redshift quasar host galaxies and the high-redshift SMG HFLS3 (Riechers et al. 2013). VB exhibits the physical characteristics of a normal (or even non-star-bursting) galaxy.

(A color version of this figure is available in the online journal.)

ratios of VB are not as well constrained, but indicate that the component is much lower density and less vigorous in star formation. The wide dispersion of individual components within HLS0918 in Figure 8 highlights the general difficulty in interpreting the location of composite (integrated) sources in such a plot.

We now explore the full complement of observed lines, while remembering that differential magnification will distort luminosity ratios involving both low- and high-J ^{12}CO lines. Figure 9 presents the individual luminosity ratios involving [C II], the $J_{upper} = (1, 2, 6, 7)$ ^{12}CO transitions, and L_{FIR} as a function of n and G_0 (the K99 model). We convert the allowed parameter space for each line ratio into a probability distribution and derive the likelihood of each n–G_0 combination, also displayed in Figure 9. The maximum likelihood from the K99 model solution is well constrained. In contrast, the M07 models consider a more complex geometry than K99 and are specifically tailored for systems with concentrated emission from galaxy centers and AGNs, but do not predict L_{FIR}. Furthermore, interpretation using the M07 models is impeded by a rather degenerate maximum likelihood solution, dominated by high-J ratios with severely non-linear tracks in n–G_0 space.

We concentrate on interpreting the K99 model contours in Figure 9. We remember that the K99 models cannot be applied directly at high redshift, where there is a warmer CMB temperature. For each line ratio, we have applied the corrections introduced above. However, these corrections are medians over the full range of likely gas densities (the plotted range in Figure 9). In reality, the corrections for CMB heating are a function of the gas density itself and should be significantly larger at lower gas densities. To test the validity of the median corrections, we return to the RADEX code and this time calculate the maximum likelihood gas density, given the observed line

ratios and once again assuming $T_k = 40$ K. We find that the gas densities are systematically half a dex lower than estimated via the PDR model (for the integrated source, $n = 10^{3.9\pm0.2}$ cm^{-3} compared with $n \approx 10^{4.3}$ cm^{-3} from Figure 9), but within the 3σ contours. However, the RADEX method includes only line ratios and ignores L_{FIR} as a constraint, as is the case for the M07 PDR models. In Figure 9, the M07 solution also favors a much lower gas density than K99, so we do not know to what extent the lower gas density from RADEX is due to CMB heating. In the following qualitative discussion, we consider the K99 PDR solution and any conclusions are robust against the possible ∼0.5 dex overestimation of n.

Components Ra, Rb, and B appear to exhibit very similar PDR characteristics. As both critical density and excitation energy increase with increasing J, higher-J ^{12}CO transitions trace the denser regions and ratios involving their luminosity are naturally located toward higher n in the diagnostic plot. The $L_{CO(2-1)}/L_{CO(1-0)}$ contour is parallel to these, but at lower n, which suggests that ^{12}CO(1–0) is the most extended. From observations of three quasar host galaxies at $z \sim 4$, Riechers et al. (2006) estimated that an extended molecular gas component could contribute up to 30% of the overall emission line luminosity of ^{12}CO(1–0). Unfortunately, the spatial resolution of the ^{12}CO(1–0) map for HLS0918 hampers the direct detection of extended ^{12}CO emission, showing no significant structure beyond the SMA 1 mm continuum map convolved by the VLA restoring beam. However, if we assume that extended emission accounts for 30% of the observed flux, the densest PDR regions (i.e., 70%–75% of ^{12}CO(1–0); 100% of higher-J lines) presents a single-phase solution, suggesting a compact, uniform star-forming nucleus.

The other interesting discrepancy is the $L_{[C\,II]}/L_{CO(1-0)}$ contour, which lies at significantly lower G_0 than the peak

13
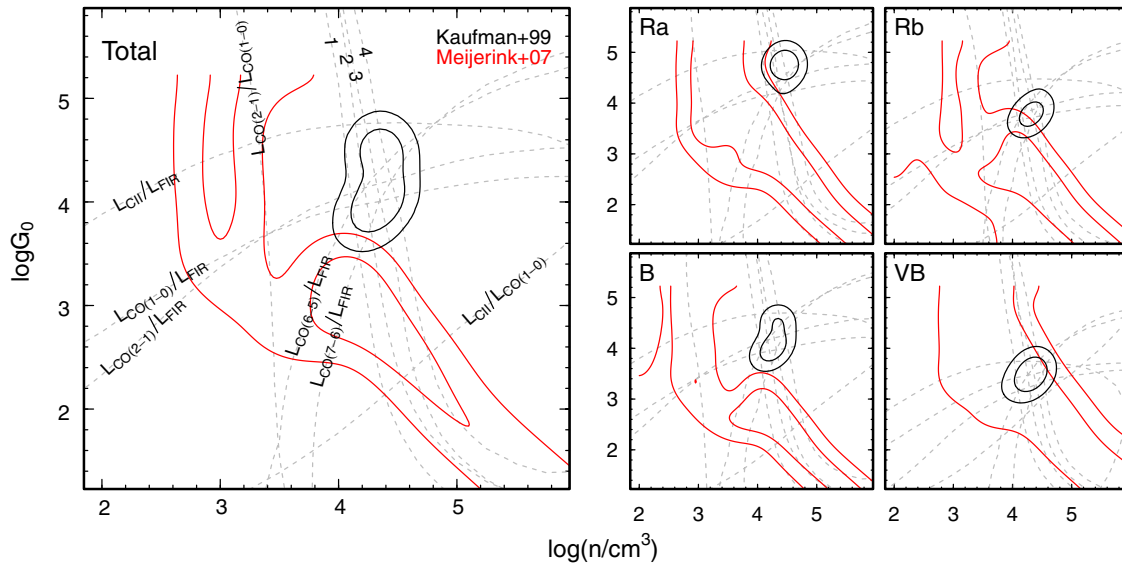
Figure 9. HLS0918 luminosity ratios involving ^{12}CO, [C II], and $L_{FIR(42.5-122.5\,\mu m)}$ (dashed lines) as a function of gas density (n) and incident FUV flux (G_0, in units of Habing field), from the PDR models of K99. The observed ratios have been adjusted to account for the non-negligible CMB heating at $z = 5.24$. The correction factors may be underestimated at the lowest gas densities (see the text for further details). For clarity, the ratios $L_{CO(6-5)}/L_{CO(1-0)}$, $L_{CO(7-6)}/L_{CO(1-0)}$, $L_{CO(6-5)}/L_{CO(2-1)}$, and $L_{CO(7-6)}/L_{CO(2-1)}$ are labeled 1, 2, 3, and 4, respectively. The black solid contours show the peak likelihood solution for the K99 models, while the red contours show similar contours from the less well-constrained M07 PDR models (including only [C II] and ^{12}CO transitions). The main (left) panel presents the integrated system, while on the right side, the four individual components are shown. Ra, Rb, and B exhibit very similar PDR diagnostic plots as the total system, exhibiting characteristics suggestive of extended $^{12}CO(1-0)$ and [C II] gas. The diagnostic diagram of the VB component is striking for a possible single-phase solution.

(A color version of this figure is available in the online journal.)

likelihood solution. This suggests that there may also be [C II] emission arising from a low-density, cold, neutral ISM component, as proposed by, e.g., Madden et al. (1993), who observed as much as 50% of [C II] originating from beyond the dense PDR. HLS0918, as well as many other high-redshift galaxies, exhibits a larger $L_{[C II]}/L_{FIR}$ for a given FIR luminosity than the local star-forming galaxies (Figure 6). An extended [C II] reservoir that surrounded star-forming regions at high redshift, but is lacking from the more evolved local galaxies (possibly through stripping or quenching processes), would account for such an offset. Indeed, remove 50% from the observed $L_{[C II]}$ and components Ra, Rb, and B would lie very close to the local galaxy population mean in Figure 6.

The VB component exhibits a marginally lower gas density and G_0 compared with the other components. Furthermore, there is a unique intersection of all the luminosity ratios included in the K99 models. If the multi-phase solutions for Ra, Rb, and B are due to extended [C II] and $^{12}CO(1-0)$ gas, then by the same logic the VB component PDR diagram may be interpreted as evidence for a lack of such an extended gas component. The lack of significant detections for VB in the high-J ^{12}CO lines also indicates that the gas in this component is not just at lower density, but is also cooler. We tentatively interpret this as evidence for a much less vigorously star-forming region than the intense R and Rb components (also revealed by a lower SFE) and suggest that the galaxy hosting component VB may have undergone a process whereby extended gas has been removed (e.g., stripping via interaction). However, we caution that all of the measured ^{12}CO emission in the VB component is near the limit of detection.

4.4. Interpretation of H_2O, [N II], and [C I]

The PDR analysis based on the [C II] and ^{12}CO emission tends toward a scenario in which the four components originate from the star-forming regions in a system of two to three interacting galaxies. Additional line detections shed more light on this configuration and, in the case of component VB, may provide evidence for an alternative, exotic origin.

The H_2O line profile at $304\,\mu m$ is particularly interesting for only being detected in components Ra and Rb (and not B and VB). Although water is the second most abundant oxygen-bearing molecule in the warm ISM after CO, a very high infrared radiation field is required to liberate ice through grain heating and to excite detectable emission lines. Recently, Omont et al. (2013) reported a ubiquitous power law $L_{H_2O} = L_{FIR}^\alpha$ for ULIRGs at all redshifts, where $\alpha = 1.22 \pm 0.10$ for $H_2O_p(2, 0, 2-1, 1, 1)$. Ra is consistent with this trend, exhibiting $\alpha = 1.13 \pm 0.09$. In contrast, Rb has very strong water emission relative to L_{FIR} ($\alpha = 2.5 \pm 0.7$), with a comparable intrinsic FIR luminosity to Apr 220, but three to four times the L_{H_2O}. None of the ULIRGS presented in Omont et al. exhibit such a large H_2O/FIR ratio, although a direct comparison is impossible as the sample does not include high-redshift galaxies with such a large FIR luminosity. The most likely scenario is that the strong FIR radiation from intense star formation[23] in component Ra ($L_{FIR,Ra} \approx 10^{13}\,L_\odot$ after accounting for lensing) excites water emission in both Ra and Rb, which in turn indicates that the two components are neighboring star-forming regions. The lens model indicates a source-plane separation between Ra and Rb of <1 kpc and the components have a mutual $\Delta V = 250$ km s^{-1}, which is consistent with two regions within the nucleus of a massive galaxy.

Comparing components B and Rb, water emission is the most discrepant line. In every other line profile, B and Rb exhibit consistent ratios of Rb/B = 1.2 ± 0.1 (Figure 3). With the

---

[23] An embedded AGN might also produce the required radiation field to excite the water emission. Figure 8 indicates a resemblance between Ra and high-redshift quasar hosts, so this possibility cannot be ruled out on the current evidence. Further constraint on a possible AGN is difficult without mid-IR or optical emission line detections.

H$_2$O emission in Rb now explained via excitation through close proximity to the intense FIR radiation from Ra (which is not the case for B), the similarity in all other respects is striking. We speculate that the star formation in Rb and B was triggered by the same event, resulting in similar timescales and hence consistent physical gas properties. It is possible that B is a spiral arm or tidal tail on the outskirts of the Ra–Rb system. However, with such a large velocity offset from the "nuclear" Ra component ($\Delta V \sim 600$ km s^{-1}), it may be more likely that component B is a region of triggered nuclear star formation in a second galaxy, interacting with Ra–Rb ($\sim$1:3 major merger, based on continuum luminosity and derived gas masses). The lack of detected water emission in component B suggests that the star formation is much lower density than the nuclear Ra (e.g., M82; Duffy et al. 1987). The merger scenario is also consistent with recent studies (e.g., Engel et al. 2010) suggesting that the vast majority of SMGs are gas-rich major mergers (mass ratios of 1:3 or greater), with an increasingly large number of well-constrained examples (e.g., Tacconi et al. 2008; Danielson et al. 2011; Aguirre et al. 2013; Fu et al. 2013). The fraction of late-stage merging systems within the local ULIRG population ($\sim$64% have nuclear separations $\lesssim$2 kpc; Veilleux et al. 2002) indicates that many (unresolved) compact SMGs are recently coalesced. HLS0918, although resolved due to the strong lensing effect, falls into this category, as components Ra and B have a line-of-sight, source-plane separation of only $\sim$1 kpc.

The $L_{[N\,II]}/L_{[C\,II]}$ ratio is an indicator of ionization and potentially traces metallicity. In the local universe ($z \ll 0.1$), [N II]/[C II] is reported for only six galaxies (mean $\sim$ 0.05, ranging from 0.01 to 0.07), with *Herschel* spectroscopy providing many recent observations: M82, Mrk 231, NGC 1097, Arp 220, NGC 1068, and NGC 4559 (Petuchowski et al. 1994; Fischer et al. 2010; Beirao et al. 2010; Rangwala et al. 2011; Spinoglio et al. 2012; Croxall et al. 2012). ALMA will facilitate a similar increase in data at high redshift in the near future, but thus far, only one high-redshift $L_{[N\,II]}/L_{[C\,II]}$ measurement has been reported, for LESSJ0332 at $z = 4.76$ (Nagao et al. 2012). With the new [C II] observation from SMA and [N II] reported by C12, HLS0918 is the second high-z source with both line measurements.

The integrated HLS0918 has $L_{[N\,II]}/L_{[C\,II]} = 0.052 \pm 0.006$, which is coincidentally identical to the $L_{[N\,II]}/L_{[C\,II]} = 0.052 \pm 0.006$ reported for LESSJ0332. However, it is the deconvoluted line profile of [N II] that is particularly interesting, with a striking difference compared with the [C II] and ^{12}CO lines. Whereas $L_{[N\,II]}/L_{[C\,II]}$ is consistent within the errors for Ra, Rb, and B (0.039 $\pm$ 0.016, 0.047 $\pm$ 0.023, and 0.039 $\pm$ 0.017, respectively), component VB has a larger ratio: $L_{[N\,II]}/L_{[C\,II]} = 0.12 \pm 0.07$. Even though the formal uncertainty from the fit is high, the luminosity ratio of VB is visibly larger in the plotted profiles (Figure 3), due to the exceptionally bright [N II] emission.

An enhanced [N II]/[C II] ratio may indicate a high metallicity. From the models presented in Nagao et al. (2012), we estimate a gas metallicity for VB of $\sim$2–3 $Z/Z_\odot$, whereas the other components appear to be approximately solar metallicity. Although high-redshift galaxies are generally expected to be less enriched than local counterparts, an intensely active system such as HLS0918 may have significantly enriched gas, although it is not clear why this should strengthen the [N II] emission of only component VB, which we have already shown to be the least efficient star-forming clump in HLS0918. Furthermore, the Nagao et al. (2012) models do not account for [C II] dependence

on age or a contribution from AGNs and Contini et al. (2002) show that N/O (and, by extension, N/C) may be a poor tracer of metallicity in starbursts and at high redshift, as gas tends to be enriched in primary elements rather than N. The PDR analysis shows that component VB is diffuse and cooler than the other components, which indicates that VB may be a third galaxy in the group, too distant from Ra–Rb and B to have such vigorous triggered nuclear star formation.

There is, however, another possible interpretation of component VB. The emission profiles of B and VB are very different, as VB has strong low-J ^{12}CO lines, as well as relatively bright ionized gas lines, [C I] and [N II]. These pointers and, in particular, the high N/CO ratio, indicate that VB may be a high-velocity, ionized outflow. Such an outflow could conceivably be driven by the high radiation pressure produced by the intense FIR field that we have already invoked for the H$_2$O emission. Molecular outflows are particularly enticing, as they represent the quenching mechanism in action, expelling fuel from star-forming nuclei. Tentative evidence for high-redshift massive outflows powered by quasar activity has recently been presented for a system at $z = 6.4$ (Maiolino et al. 2012). The situation is no clearer for the $z = 4.7$ merger BR1202-0725, which has a quasar host galaxy as a close companion, where two recent analyses of the ALMA [C II] data differ significantly in their conclusions concerning the existence of an outflow (e.g., Wagg et al. 2012; Carniani et al. 2013). In HLS0918, the derived conditions are not so extreme as to rule out VB simply being a third galaxy rather than an outflow. Before either scenario can be adopted, further observations are required, such as maps of, e.g., OH$^+$, CH$^+$, and H$_2$O$^+$. Such species are excellent tracers of molecular outflows and have been reported for several local ULIRGs, e.g., Arp 220, (Rangwala et al. 2011) and Mrk 231 (van der Werf et al. 2010).

5. CONCLUSIONS

We present new maps of the [C II] (from the SMA) and ^{12}CO(1–0) (from the VLA) emission for HLS0918, a $z = 5.2430$ lensed SMG behind A773. These observations are combined with previously reported line profiles including multiple ^{12}CO rotational transitions, [C I], water, and [N II] (C12). We briefly describe a new lens model, including the contribution from both A773 ($\sim$10%) and a foreground galaxy at $z = 0.62$, and derive a total magnification $\mu_{\rm total} = 8.9 \pm 1.9$. A detailed description of the lens model will be presented in F. Boone et al. (in preparation). The total FIR luminosity is $L_{\rm FIR,demag} = (1.8 \pm 0.4) \times 10^{13} L_\odot$ and the updated FIR SED argues for a steep dust emissivity index ($\beta \sim 2$). Although HLS0918 is a HyLIRG, the FIR continuum shape resembles that of a local LIRG.

We discover four spectral components of HLS0918 that correspond cleanly to discrete spatial structures identified in the maps. The four components originate from a source-place region separated by $\lesssim$4 kpc, with the three reddest crossing the caustic (double images).

The reddest spectral component (Ra; $V \sim +120 \pm 30$ km s^{-1}) has a demagnified $L_{\rm FIR,Ra,demag} = (1.1 \pm 0.2) \times 10^{13} L_\odot$, dominating the continuum map, and exhibits a very high SFE of $360 \pm 90 L_\odot M_\odot^{-1}$. Both Ra and the second most redshifted component (Rb; $V \sim -130 \pm 20$ km s^{-1}; $L_{\rm FIR,Rb,demag} = (1.9 \pm 0.4) \times 10^{12} L_\odot$) show strong water emission, possibly excited by the powerful FIR radiation field caused by the intense star formation of Ra, and likely form the nucleus of a massive galaxy.

A third component (B; -470 ± 10 km s^{-1}) is intrinsically twice as luminous as Rb ($L_{\mathrm{FIR,B,demag}} = (4.0 \pm 0.8) \times 10^{12}\,L_\odot$), appearing as an eastern bridge in the continuum map. Water emission is undetected in B, but otherwise the component exhibits a stable luminosity ratio with Rb (Rb/B $\sim 1.2 \pm 0.1$). B is most likely a star-forming region in a second, merging companion to the Ra–Rb galaxy, with a nuclear separation of only ~ 1 kpc. Components Ra, Rb, and B all show evidence of an extended ^{12}CO(1–0) and [C II] reservoir around the densest star-forming PDR. The elevated [C II] from the diffuse gas explains the observed offset from local ULIRGs: more evolved systems that presumably lack such an extended gas reservoir. On the other hand, the gas properties and morphology of HLS0918 exhibit strong evidence that the Ra–Rb/B system is a late-stage merger, consistent with the majority of local ULIRGs.

The faint, bluest component (VB; $V \sim -720 \pm 40$ km s^{-1}; $L_{\mathrm{FIR,VB,demag}} = (4.5 \pm 0.9) \times 10^{11}\,L_\odot$) originates from a spatially distinct region, which appears to be lower density, cooler, and less vigorously forming stars than the other components. The component may also lack an extended molecular gas component, perhaps suggesting a less active companion galaxy that has recently undergone an interaction. However, VB exhibits strikingly bright ionized gas lines ([N II] and [C I]) and a lack of emission in high-J ^{12}CO transitions. The high N/CO ratio, in particular, could instead indicate that the component originates from an ionized, molecular outflow. Observation of additional species known to trace molecular outflows (e.g., OH$^+$, CH$^+$, H$_2$O$^+$) are required to confirm this scenario.

This comprehensive view of the gas properties and morphology of a system at $z = 5.2$ shows the power of gravitational lensing in revealing star formation and galaxy evolution in the early universe. This paper also offers a preview of the type of analysis that will become possible for a large number of high-redshift galaxies once ALMA progresses to full science operations.

REFERENCES

Aguirre, P., Baker, A. J., Menanteau, F., Lutz, D., & Tacconi, L. J. 2013, ApJ, 768, 164
Baker, A. J., Tacconi, L. J., Genzel, R., Lehnert, M. D., & Lutz, D. 2004, ApJ, 604, 125
Beirao, P., Armus, L., Appleton, P. N., et al. 2010, A&A, 518, 60
Blain, A. W. 1999, Ap&SS, 266, 261
Bryant, P. M., & Scoville, N. Z. 1996, ApJ, 457, 678
Carilli, C. L., Daddi, E., Riechers, D., et al. 2010, ApJ, 714, 1407
Carniani, S., Marconi, A., Biggs, A., et al. 2013, A&A, 559, 29
Chapman, S. C., Blain, A. W., Smail, I., & Ivison, R. J. 2005, ApJ, 622, 772
Clements, D. L., Dunne, L., & Eales, S. 2010, MNRAS, 403, 274
Combes, F., Garcia-Burillo, S., Braine, J., et al. 2011, A&A, 528, 124
Combes, F., Garcia-Burillo, S., Braine, J., et al. 2013, A&A, 550, 41
Combes, F., Rex, M., Rawle, T. D., et al. 2012, A&A, 538, 4 (C12)
Contini, T., Treyer, M. A., Sullivan, M., & Ellis, R. S. 2002, MNRAS, 330, 75
Coppin, K. E. K., Chapman, S. C., Smail, I., et al. 2010, MNRAS, 407, 103
Coppin, K. E. K., Swinbank, A. M., Neri, R., et al. 2007, ApJ, 665, 936
Cox, P., Krips, M., Neri, R., et al. 2011, ApJ, 740, 63
Croxall, K. V., Smith, J. D., Wolfire, M. G., et al. 2012, ApJ, 747, 81
da Cunha, E., Groves, B., Walter, F., et al. 2013, ApJ, 766, 13
Danielson, A. L. R., Swinbank, A. M., Smail, I., et al. 2011, MNRAS, 410, 1687
De Breuck, C., Maiolino, R., Caselli, P., et al. 2011, A&A, 530, 8
Decarli, R., Walter, F., Neri, R., et al. 2012, ApJ, 752, 2
Duffy, P. B., Erickson, E. F., Haas, M. R., & Houck, J. R. 1987, ApJ, 315, 68
Egami, E., Rex, M., Rawle, T. D., et al. 2010, A&A, 518, 12
Engel, H., Tacconi, L. J., Davies, R. I., et al. 2010, ApJ, 724, 233
Fischer, J., Sturm, E., Gonzlez-Alfonso, E., et al. 2010, A&A, 518, 41
Freundlich, J., Combes, F., Tacconi, L. J., et al. 2013, A&A, 553, 130
Fu, H., Cooray, A., Feruglio, C., et al. 2013, Natur, 498, 338
Genzel, R., Tacconi, L. J., Gracia-Carpio, J., et al. 2010, MNRAS, 407, 2091
Gerin, M., & Phillips, T. G. 1998, ApJ, 509, 17
Greve, T. R., Bertoldi, F., Smail, I., et al. 2005, MNRAS, 359, 1165
Griffin, M., Abergel, A., Abreu, A., et al. 2010, A&A, 518, L3
Hwang, H. S., Elbaz, D., Magdis, G., et al. 2010, MNRAS, 409, 75
Ivison, R. J., Papadopoulos, P. P., Smail, I., et al. 2011, MNRAS, 412, 1913
Ivison, R. J., Smail, I., Papadopoulos, P. P., et al. 2010a, MNRAS, 404, 198
Ivison, R. J., Swinbank, A. M., Swinyard, B., et al. 2010b, A&A, 518, 35
Jones, T. A., Swinbank, A. M., Ellis, R. S., Richard, J., & Stark, D. P. 2010, MNRAS, 404, 1247
Jullo, E., Kneib, J.-P., Limousin, M., et al. 2007, NJPh, 9, 447
Kaufman, M., Wolfire, M., Hollenbach, D., & Luhman, M. 1999, ApJ, 527, 795
Kennicutt, R. C., Jr. 1998, ARA&A, 36, 189
Kovacs, A. 2008, Proc. SPIE, 7020, 70201S
Kroupa, P. 2002, Sci, 295, 82
Levshakov, S. A., Combes, F., Boone, F., et al. 2012, A&A, 540, 9
Madden, S. C., Geis, N., Genzel, R., et al. 1993, ApJ, 407, 579
Maiolino, R., Cox, P., Caselli, P., et al. 2005, A&A, 440, 51
Maiolino, R., Gallerani, S., Neri, R., et al. 2012, MNRAS, 425, 66
Malhotra, S., Kaufman, M. J., & Hollenbach, D. 2001, ApJ, 561, 766
Meijerink, R., Spaans, M., & Israel, F. P. 2007, A&A, 461, 793
Momjian, E., Carilli, C. L., & Petric, A. O. 2005, AJ, 129, 1809
Morton, D. C., & Noreau, L. 1994, ApJS, 95, 301
Nagao, T., Maiolino, R., De Breuck, C., et al. 2012, A&A, 542, 34
Narayanan, D., Krumholz, M. R., Ostriker, E. C., & Hernquist, L. 2011, MNRAS, 418, 664
Nguyen, H. T., Schulz, B., Levenson, L., et al. 2010, A&A, 518, L5
Omont, A., Yang, C., Cox, P., et al. 2013, A&A, 551, 115
Panuzzu, P., Rangwala, N., Rykala, A., et al. 2010, A&A, 518, 37
Papadopoulos, P. P., van der Werf, P., Isaak, K., & Xilouris, E. M. 2010, ApJ, 715, 775
Petuchowski, S. J., Bennett, C. L., Haas, M. R., et al. 1994, ApJ, 427, 17
Pilbratt, G., Riedinger, J. R., Passvogel, T., et al. 2010, A&A, 518, L1
Rangwala, N., Maloney, P. R., Glenn, J., et al. 2011, ApJ, 743, 94
Rex, M., Rawle, T. D., Egami, E., et al. 2010, A&A, 518, 13
Riechers, D. A., Bradford, C. M., Clements, D. L., et al. 2013, Natur, 496, 329
Riechers, D. A., Carilli, C. L., Walter, F., & Momjian, E. 2010, ApJ, 724, 153
Riechers, D. A., Walter, F., Bertoldi, F., et al. 2009, ApJ, 703, 1338
Riechers, D. A., Walter, F., Carilli, C. L., et al. 2006, ApJ, 650, 604
Riechers, D. A., Walter, F., Carilli, C. L., Bertoldi, F., & Momjian, E. 2008, ApJ, 686, 9

Rieke, G. H., Alonso-Herrero, A., Weiner, B. J., et al. 2009, ApJ, 692, 556
Salomé, P., Guélin, M., Downes, D., et al. 2012, A&A, 545, 57
Sargsyan, L., Lebouteiller, V., Weedman, D., et al. 2012, ApJ, 755, 171
Sault, R. J., Teuben, P. J., & Wright, M. C. H. 1995, in ASP Conf. Ser. 77, Astronomical Data Analysis Software and Systems IV, ed. R. A. Shaw, H. E. Payne, & J. J. E. Hayes (San Francisco, CA: ASP), 433
Schinnerer, E., Carilli, C. L., Capak, P., et al. 2008, ApJ, 689, 5
Scoville, N. Z. 2004, in ASP Conf. Ser. 320, The Neutral ISM in Starburst Galaxies, ed. S. Aalto, S. Huttemeister, & A. Pedlar (San Francisco, CA: ASP), 253
Serjeant, S. 2012, MNRAS, 424, 2429
Solomon, P. M., & Vanden Bout, P. A. 2005, ARA&A, 43, 677
Spinoglio, L., Pereira-Santaella, M., Busquet, G., et al. 2012, ApJ, 758, 108
Stacey, G. J., Geis, N., Genzel, R., et al. 1991, ApJ, 373, 423
Stacey, G. J., Hailey-Dunsheath, S., Ferkinhoff, S., et al. 2010, ApJ, 724, 957
Staguhn, J., Allen, C., Benford, D., et al. 2008, JLTP, 151, 709
Stark, D. P., Ellis, R. S., Chiu, K., Ouchi, M., & Bunker, A. 2010, MNRAS, 408, 1628
Swinbank, A. M., Karim, A., Smail, I., et al. 2012, MNRAS, 427, 1066

Swinbank, A. M., Smail, I., Longmore, S., et al. 2010, Natur, 464, 733
Swinbank, A. M., Webb, T. M., Richard, J., et al. 2009, MNRAS, 400, 1121
Tacconi, L. J., Genzel, R., Smail, I., et al. 2008, ApJ, 680, 246
Tacconi, L. J., Neri, R., Genzel, R., et al. 2013, ApJ, 768, 74
Thomson, A. P., Ivison, R. J., Smail, I., et al. 2012, MNRAS, 425, 2203
van der Tak, F. F. S., Black, J. H., Schoier, F. L., Jansen, D. J., & van Dishoeck, E. F. 2007, A&A, 468, 627
van der Werf, P. P., Isaak, K. G., Meijerink, R., et al. 2010, A&A, 518, 42
van Zee, L., Salzer, J. J., & Haynes, M. P. 1998, ApJL, 497, L1
Valtchanov, I., Virdee, J., Ivison, R. J., et al. 2011, MNRAS, 415, 3473
Veilleux, S., Kim, D.-C., & Sanders, D. B. 2002, ApJS, 143, 315
Venemans, B. P., McMahon, R. G., Walter, F., et al. 2012, ApJ, 751, 25
Wagg, J., Wiklind, T., Carilli, C. L., et al. 2012, ApJ, 752, 30
Walter, F., Decarli, R., Carilli, C., et al. 2012a, ApJ, 752, 93
Walter, F., Decarli, R., Carilli, C., et al. 2012b, Natur, 486, 233
Wardlow, J. L., Smail, I., Coppin, K. E. K., et al. 2011, MNRAS, 415, 1479
Weiss, A., Downes, D., Neri, R., et al. 2007, A&A, 467, 955
Weiss, A., Downes, D., Walter, F., & Henkel, C. 2005, A&A, 440, 45
Weiss, A., De Breuck, C., Marrone, D. P., et al. 2013, ApJ, 767, 88